The International Journal of Advanced Manufacturing Technology (2021) 114:1601–1621
https://doi.org/10.1007/s00170-020-06485-2

ORIGINAL ARTICLE

Cutting force prediction considering tool path curvature and torsion based on screw theory

Zerun Zhu[1] · Jiawei Wu[1] · Rong Yan[1] · Fangyu Peng[2] · Xiaowei Tang[1]

Received: 23 June 2020 / Accepted: 7 December 2020 / Published online: 31 March 2021

Abstract

There are common features such as the tool path curvature and torsion, and cutter-orientation change in sculptured surface machining, which bring new challenges to the accurate prediction of cutting force. Aiming at the tool path curvature and torsion, and cutter-orientation change, a cutting force prediction method based on the screw theory is proposed in this paper. For the first time, the screw theory is used to describe the cutter spatial motion, which includes the feed motion considering the tool path curvature and torsion, and cutter-orientation change. Combining with Frenet frame, the analytical formula of the screw of cutting edge elements is derived through the homogeneous coordinate transformation. Then, the instantaneous uncut chip thickness (IUCT) of each cutting edge element is calculated by the vector projection method. And the cutting state of the cutting edge element is determined by its IUCT and position relative to the workpiece surface, which is updated by the cutter envelope surface along the machined tool path derived with the screw. To verify the effectiveness of the proposed cutting force prediction method, a milling experiment is conducted on a conical surface workpiece along a tool path with curvature and torsion characteristics, and changing cutter-orientations. Then, the effects of the tool path curvature and torsion, and cutter-orientation change on the cutting force are simulated and analyzed. The results show that the proposed cutting force model based on the screw theory has higher prediction accuracy for the sculpture surface machining with curving and torsional tool paths and changing cutter-orientations.

Keywords Five-axis machining · Cutting force · Tool path curvature and torsion · Screw theory

Nomenclature

K, K_i	Tool path curvature
τ, τ_i	Tool path torsion
IUCT	Instantaneous undeformed chip thickness
CWE	Cutter-workpiece engagement
H	Effective axial cutting length of the cutter flute
D	Cutter diameter
r	Cutter fillet radius
N	Number of cutter flutes
β	Helix angle of the cutter flute
Q	Cutting edge element
Q_i	Cutting edge element whose coordinate in FCS is (x_F, y_F, z_F, 1) at time t_i
$O_i^{(FCS_{(i)})}$	The coordinate of Q_i in $FCS_{(i)}$
$O_{i+1}^{(FCS_{(i+1)})}$	The coordinate of Q_{i+1} in $FCS_{(i+1)}$
z	Axial position of Q
$r(z)$	Effect cutting radius of Q
κ, κ_i	Axial contact angle of Q
φ, φ_i	Radial location angle of Q
ψ	Cutter rotation angle
$\psi(z)$	Radial lag angle
$\boldsymbol{n}$	Unit normal vector of the tool surface at Q
O_W-X_W-Y_W-Z_W	Workpiece coordinate system (WCS)
O_T-X_T-Y_T-Z_T	Tool coordinate system (TCS)
O_F-X_F-Y_F-Z_F	Feed coordinate system (FCS)
DS	Design surface of the workpiece

✉ Rong Yan
yanrong@hust.edu.cn

[1] National NC System Engineering Research Center, School of Mechanical Science and Engineering, Huazhong University of Science and Technology, 1037 Luoyu Road, Wuhan 430074, China

[2] State Key Laboratory of Digital Manufacturing Equipment and Technology, School of Mechanical Science and Engineering, Huazhong University of Science and Technology, 1037 Luoyu Road, Wuhan 430074, China

$lead$, $lead_i$	Lead angle
$tilt$, $tilt_i$	Tilt angle
l	Lead angle change rate
t	Tile angle change rate
O_F	Tangent point between the tool surface and DS
$O_F^{(TCS)}$	The cutting contact point O_F in TCS
${}^{FCS}_{TCS}\boldsymbol{R}$	Rotation transformation matrix from TCS to FCS
${}^{TCS}_{FCS}\boldsymbol{T}$	Homogeneous coordinate transformation matrix from FCS to TCS
${}^{WCS}_{FCS}\boldsymbol{T}$	Homogeneous coordinate transformation matrix from FCS to WCS
$\boldsymbol{r}(s)$	Natural parameter equation of tool path Γ
$\{\boldsymbol{r}_i, \boldsymbol{\alpha}_i, \boldsymbol{\beta}_i, \boldsymbol{\gamma}_i\}$	Frenet frame of Γ at point $\boldsymbol{O}_{F(i)}$
$Fra_{(i)}$	Cartesian coordinate system formed by $\{\boldsymbol{r}_i, \boldsymbol{\alpha}_i, \boldsymbol{\beta}_i, \boldsymbol{\gamma}_i\}$
${}^{FCS_{(i)}}_{FCS_{(i+1)}}\boldsymbol{T}$	Homogeneous coordinate transformation matrix from $FCS_{(i+1)}$ to $FCS_{(i)}$
${}^{FCS_{(i)}}_{Fra_{(i)}}\boldsymbol{T}$	Homogeneous coordinate transformation matrix from $Fra_{(i)}$ to $FCS_{(i)}$
${}^{Fra_{(i)}}_{Fra_{(i)}}\boldsymbol{T}$	Homogeneous coordinate transformation matrix from $Fra_{(i+1)}$ to $Fra_{(i)}$
${}^{Fra_{(i+1)}}_{FCS_{(i+1)}}\boldsymbol{T}$	Homogeneous coordinate transformation matrix from $FCS_{(i+1)}$ to $Fra_{(i+1)}$
$\Delta\boldsymbol{\alpha}$, $\Delta\boldsymbol{\beta}$, $\Delta\boldsymbol{\gamma}$, $\Delta\boldsymbol{r}$	Change in coordinates of Frenet frame $\{\boldsymbol{r}_i, \boldsymbol{\alpha}_i, \boldsymbol{\beta}_i, \boldsymbol{\gamma}_i\}$
Δs	The arc length differential of the tool path
v_f	The tool feed rate
Δt	Time step
$[V_F]$, $[V_T]$	The screw representing the cutter spatial motion in FCS, TCS
$\boldsymbol{v}_F$, $\boldsymbol{v}_T$	Line velocity of $[V_F]$, $[V_T]$
$\boldsymbol{\omega}_F$, $\boldsymbol{\omega}_T$	Angular velocity of $[V_F]$, $[V_T]$
h_F, h_T	Pitch of $[V_F]$, $[V_T]$
$\boldsymbol{r}_F$, $\boldsymbol{r}_T$	The orthogonal position vector and satisfies $\boldsymbol{\omega}_F \perp \boldsymbol{r}_F$, $\boldsymbol{\omega}_T \perp \boldsymbol{r}_T$
$(\theta\omega_1)\otimes\boldsymbol{R}_P$	the rotation of $\boldsymbol{R}_P$ around $\boldsymbol{\omega}_1$ by θ
h_Q	The IUCT of Q
$\boldsymbol{n}_Q$	Unit normal vector of the tool surface at point Q
$\Pi_i^{(TCSi)}$	Cluster of the points on the cutter envelope surface in $TCS_{(i)}$ for $t \in [t_i, t_{i+1}]$
$\Pi^{(WCS)}$	Cluster of the points on the cutter envelope surface of each time period in a tool path
dF_t, dF_r, dF_a	The tangential, radial, and axial chip load of cutting edge element Q
K_t, K_r, K_a	The tangential, radial, and axial cutting force coefficients
dF_x, dF_y, dF_z	Chip loads of Q in TCS
F_x, F_y, F_z	Instantaneous milling force

1 Introduction

In the aerospace industry, five-axis end milling is widely used in the machining of complex structural and surface parts such as aero-engine impellers, blisks, and blades, to avoid the interference between cutters and workpieces. In the above-mentioned processing, such as the turning and milling of aero-engine blades [1] and the machining of aero-engine blisks with cycloidal trajectories [2], the tool path curvature and torsion, and cutter-orientation change often appear, which could be a considerable influence on the cutting force [3, 4]. Taking the milling of an aero-engine blade in Fig. 1 as an example, it can be seen that the cutter-orientation changes dramatically. In the close-up on the right, $\{\mathbf{r}; \boldsymbol{\alpha}, \boldsymbol{\beta}, \boldsymbol{\gamma}\}$ is the Frenet frame of the tool path curve, and K and τ are the curvature and torsion, respectively. The tool path curvature describes the bending degree of the tool path curve, and the tool path torsion describes the degree of distortion of the tool path curve away from the osculating plane. The cutting force is an important factor that affects the machining accuracy [5], tool life, and machining vibration. The prediction accuracy of cutting force is of great significance to the optimization of process parameters [6]. Therefore, it is necessary to establish a five-axis milling force model that can take into account the tool path curvature and torsion, and cutter-orientation change for sculptured surface machining.

The mechanistic models are widely used in the five-axis milling force modeling, the most important of which are the modeling of IUCT and cutter-workpiece engagement (CWE). The tool path curvature and torsion, and cutter-orientation change determine the spatial motion trajectory of cutting edge elements and affect IUCT and CWE, becoming non-negligible factors affecting the cutting force.

In five-axis milling, the commonly used IUCT modeling methods are the vector projection method and the geometrical calculation method [7]. The vector projection method is to project the feed vector onto the outer unit normal vector of the tool surface to obtain IUCT. For example, Fussell et al. [8] decomposed the velocity of cutting edge elements into the feeding velocity of tool center and the angular velocity of the cutting tool resulting from the rotational axes of NC

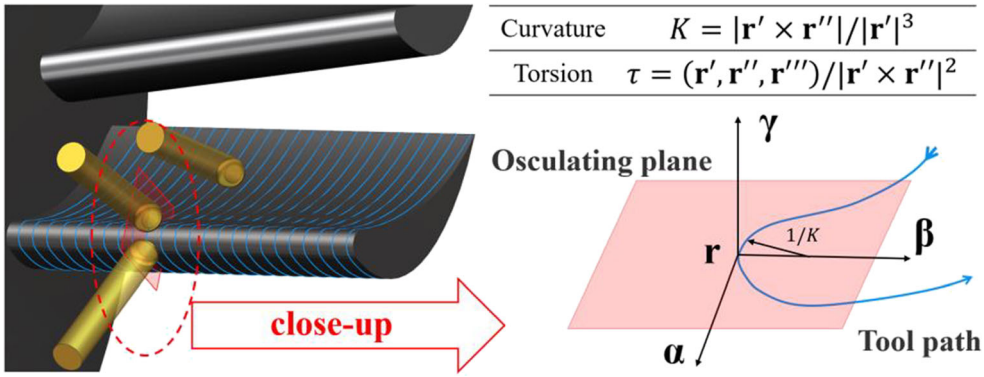

Fig. 1 Tool path curvature and torsion, and cutter-orientation change in milling

machine. Zhu et al. [7] proposed the cutting edge element moving (CEEM) method. Wang et al. [9] calculated the feed vectors of cutting edge elements according to the two adjacent tool positions. Duan et al. [10] accurately analyzed the translation and rotation of the cutting edge elements. All the above works were to obtain the feed vector more accurately for higher precision of IUCT. Wu et al. [11] also analyzed the effect of tool path curvature on IUCT in circular end milling. The geometrical calculation method is to calculate the segment length between the current cutting edge element and the cutter edge trajectory sweeping surface of the front cutting edge along the IUCT defined line. Zhu et al. [12] simulated the tool motion by interpolation of the tool location file, and defined the distance from the instantaneous position of the cutting edge element to the tool envelope a tooth passing period ago as IUCT. By analyzing the relative motion of the cutter-workpiece, Sun et al. [13] proposed an IUCT model of ball-end milling that can be employed for any cases of tool path and varying feed rate. Li et al. [14] made a circular assumption for the trochoid tooth trajectory, which significantly improved the simulation efficiency of the IUCT while ensuring the prediction accuracy. From a comprehensive perspective, the vector projection method has higher computational efficiency and lower accuracy than the geometrical calculation method. Wojciechowski and Mrozek [15] established an IUCT model considering run out, minimum IUCT, and kinematics of low radial immersion milling with tool axis inclination, and further considering the chip thickness accumulation for higher cutting force simulation accuracy [16]. Although some of the previous studies have analyzed the translation and rotation of cutting edge elements [8, 10], none of them can reveal the essential reasons affecting the IUCT, which is analyzed in this paper by the screw model. In this paper, the method of calculating IUCT is developed with the vector projection method based on the screw, which can fully consider the influence of the tool path curvature and torsion, and cutter-orientation change on the cutter spatial motion, thereby improving the calculation accuracy of the IUCT in the corresponding machining conditions.

The role of CWE is to determine the cutting state of cutting edge elements. There are generally three methods to determine CWE in five-axis machining [17]. The first are the solid model Boolean subtraction algorithms based on ACIS or Parasolid kernel [18–20]. The second are the analytical methods, which mainly depend on the approximation of the workpiece surface information by using the cutter location file [21]. Kiswanto et al. [22] calculated the lower engagement point and the upper engagement point to obtain CWE for the step workpiece surface left by semi-finishing. The third are the discrete modeling methods, which obtain CWE by discretizing the cutter surface and workpiece surface, such as z-buffer [8], Octree [23], dexel [24], and the most commonly used z-map [3, 7, 10, 12, 25]. Cao et al. [26] and Yuan et al. [27] calculated CWE considering the surface curvature and cutter orientations. In CWE modeling, most studies simplify tool motion to be linear [14, 17, 22], ignoring the tool path curvature and torsion, and cutter-orientation change, which affects the accuracy of cutting state judgment of cutting edge elements.

The screw theory has a simple and clear way of describing the rigid body spatial motion and is easy to solve the kinematics. It is an important tool in the research of mechanism and robotics [28, 29], and it has also been gradually applied in the geometric error modeling of machine tools in recent years [30, 31]. Based on the advantages of the screw in kinematics description, this paper first employs it for describing tool motion in milling, with the tool path curvature and torsion, and cutter-orientation change considered.

In this paper, a cutting force prediction method considering the tool path curvature and torsion, and cutter-orientation is developed based on the screw theory. First, the screw model that can accurately describe the cutter spatial motion is established considering the effect of the tool path curvature and torsion, and cutter-orientation change. Then, based on the cutter motion model, the IUCT is calculated with the vector projection method, and the cutting state of the cutting edge elements is determined combining with their position relative to the workpiece surface. Finally, the proposed cutting force model is verified by the five-axis

machining experiment, and the effects of the tool path curvature and torsion, and cutter-orientation change on the cutting force are simulated and their essential causes are analyzed. Compared with the previous works, the main contributions of this paper are as follows:

1. For the five-axis machining considering the tool path curvature and torsion, and cutter-orientation change, the screw model that can accurately describe the cutter spatial motion is analytically derived;
2. Based on the screw, the IUCT is calculated by the vector projection method with the effect of the tool path curvature and torsion, and cutter-orientation change;
3. Based on the screw, the solution formula of the cutter envelope surface is derived and the method of workpiece surface updating is proposed to determine the CWE.
4. The effects of the tool path curvature and torsion, and cutter-orientation change on the cutting force under the set machining conditions are simulated respectively, and the essential causes of cutting force change are analyzed.

The remainder of this paper is organized as follows. In Section 2, the screw model based on the tool trajectory is established. In Section 3, the IUCT is obtained based on the screw, and the methods of judging the cutting state of the cutting edge elements and updating the workpiece surface are proposed. In Section 4, the algorithm flow chart of cutting force simulation is provided. In Section 5, the verification experiment is carried out and some discussions are performed, followed by the summary and outlook in Section 6.

2 Screw modeling based on tool trajectory

This section mainly defines the geometric parameters of the fillet cutter and the coordinate transformation relationship between the cutter coordinate system, the feed coordinate system, and the workpiece coordinate system. Based on the screw theory, the tool motion related to the curvature and torsion of the tool path, and the one related to the cutter-orientation change are modeled and analyzed, respectively. As a result, the tool motion model in complex tool trajectory is obtained.

2.1 Geometric and coordinate system models

2.1.1 Geometry of a bullnose end cutter

Figure 2 describes the bullnose end cutter model and parameters in the tool coordinate system (TCS). The tool is divided into two zones: the arc zone and the side zone. The cutter geometry is determined by five parameters: $\{H, D, r, N, \beta\}$, where H is the effective axial cutting length of the cutter flute, D is the cutter diameter, r is the fillet radius, N is the number of cutter flutes, and β is the helix angle ($\beta > 0$ means dextrorotatory). Then, any cutting edge element Q can be expressed in TCS as:

$$Q = [r(z)\sin(\varphi), r(z)\cos(\varphi), z]^{\mathrm{T}} \tag{1}$$

where z is the axial position of Q, $r(z)$ is the distance from Q to Z_{T}-axis, i.e., the effective cutting radius, and is expressed as:

$$r(z) = \frac{D}{2} - r + r\sin(\kappa) \tag{2}$$

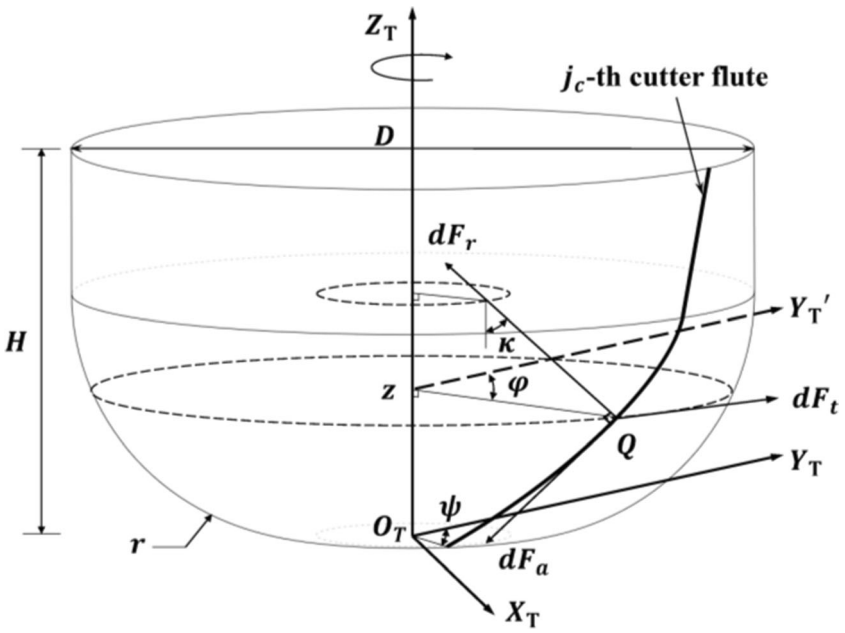

Fig. 2 The bullnose end cutter model and parameters in TCS

where κ and φ are the axial contact angle and the radial location angle of Q respectively and can be formulated as:

$$\kappa = \begin{cases} \arccos\left(\frac{r-z}{r}\right) & 0 \le z \le r \\ \frac{\pi}{2} & r < z \le H \end{cases} \tag{3}$$

$$\varphi = \psi + (j_c - 1)\frac{2\pi}{N} - \psi(z) \tag{4}$$

where j_c is the serial number of the flute, ψ is the cutter rotation angle, and $\psi(z)$ is the radial lag angle and can be obtained by:

$$\psi(z) = \frac{2z\tan\beta}{D} \tag{5}$$

Then, the outer unit normal vector of the tool surface at Q can be expressed in TCS as:

$$\mathbf{n} = [\sin(\varphi)\sin(\kappa) \;\; \cos(\varphi)\sin(\kappa) \;\; -\cos(\kappa)]^{\mathrm{T}} \tag{6}$$

2.1.2 Coordinate systems and their transformation relationship

Figure 3 describes the relative position of the tool and the workpiece, where DS represents the design surface. $O_W - X_W - Y_W - Z_W$ is the workpiece coordinate system (WCS). $O_F - X_F - Y_F - Z_F$ is the feed coordinate system (FCS), where point O_F is the tangent point between the tool surface and DS (i.e., the cutter contact point), Z_F-axis is the tool side unit normal vector of DS at point O_F, and X_F-axis is a unit vector along the direction of instantaneous feed velocity.

The cutter orientation in FCS can be described by the lead angle and tilt angle (denoted as *lead* and *tilt* respectively). The rotation transformation from FCS to TCS is shown in Fig. 4: FCS rotates around Y_F-axis by angle "*lead*" to become the transitional coordinate system $O' - X' - Y' - Z'$, and $O' - X' - Y' - Z'$ rotates around X_F-axis by angle *tilt* to become TCS. Then, the rotation transformation matrix from TCS to FCS is:

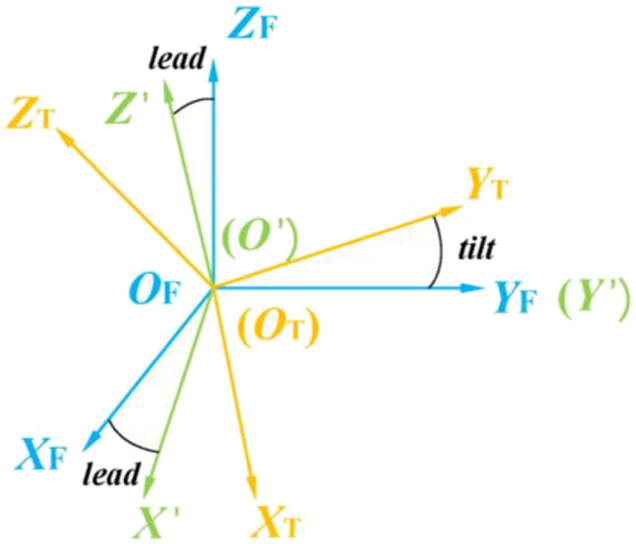

Fig. 4 Rotation transformation from TCS to FCS

$$ {}^{\mathrm{FCS}}_{\mathrm{TCS}}\boldsymbol{R} = \begin{bmatrix} 1 & 0 & 0 \\ 0 & \cos(tilt) & -\sin(tilt) \\ 0 & \sin(tilt) & \cos(tilt) \end{bmatrix} \cdot \begin{bmatrix} \cos(lead) & 0 & \sin(lead) \\ 0 & 1 & 0 \\ -\sin(lead) & 0 & \cos(lead) \end{bmatrix} \tag{7}$$

The homogeneous coordinate transformation matrix from FCS to TCS can be expressed as:

$$ {}^{\mathrm{TCS}}_{\mathrm{FCS}}\boldsymbol{T} = \begin{bmatrix} ({}^{\mathrm{FCS}}_{\mathrm{TCS}}\boldsymbol{R})^{-1} & O_{\mathrm{F}}^{(\mathrm{TCS})} \\ 0 & 1 \end{bmatrix} \tag{8}$$

where $O_F^{(TCS)}$ represents the coordinate of the cutter contact point O_F in TCS, which can be solved by the antiparallel

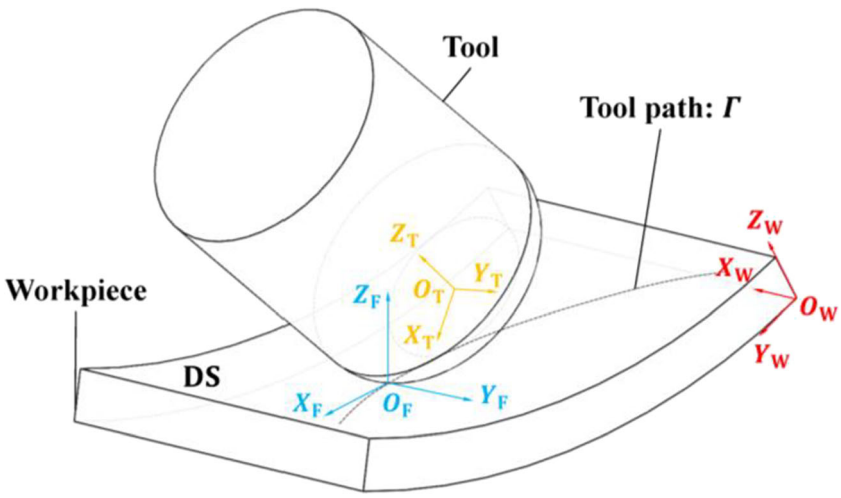

Fig. 3 Schematic of tool and workpiece

relationship between the outer normal vectors of DS and tool surface at point O_F, the specific process can be found in reference [17].

The homogeneous coordinate transformation matrix from FCS to WCS can be expressed as:

$$ {}^{\mathrm{WCS}}_{\mathrm{FCS}}\boldsymbol{T} = \begin{bmatrix} X_F^{(\mathrm{WCS})} & Y_F^{(\mathrm{WCS})} & Z_F^{(\mathrm{WCS})} & O_F^{(\mathrm{WCS})} \\ 0 & 0 & 0 & 1 \end{bmatrix} \quad (9) $$

where $X_F^{(\mathrm{WCS})}$, $Y_F^{(\mathrm{WCS})}$, and $Z_F^{(\mathrm{WCS})}$ represent the coordinates of the corresponding axis of FCS in WCS, and $O_F^{(\mathrm{WCS})}$ represents the coordinate of the origin of FCS in WCS.

2.2 Screw modeling based on the cutter spatial motion decomposition

When using the vector projection method to calculate IUCT, some studies have analyzed the translation and rotation of cutting edge elements [8, 10], while in other studies, the detailed analysis of the cutter spatial motion is rarely carried out. The purpose of this section is to accurately represent the cutter spatial motion in the form of screw. The cutter spatial motion is decomposed into two parts. One is the cutter feed motion along the tool path with a fixed inclination, and the influence of the tool path curvature and torsion, and workpiece shape are considered here. The other is the cutter-orientation change caused by the change of the tool inclination. Finally, the analytical model of tool motion spinor is established, which makes a good preparation for the modeling of IUCT and the solution of tool motion envelope.

2.2.1 Feed motion modeling

Figure 5 is the schematic of the coordinate systems on tool path Γ, which is attached to DS and can be regarded as a combination of the cutter contact points at different times. The natural parameter equation of Γ is $r = r(s)$, $O_{F(i)}$ and $O_{F(i+1)}$ are two adjacent points on it. The Frenet frame of Γ at point $O_{F(i)}$ is denoted as $\{r_i; a_i, \beta_i, \gamma_i\}$, where the four vectors represent the radius vector, tangent vector, principal normal vector, and auxiliary normal vector of Γ at point $O_{F(i)}$ respectively. The Cartesian coordinate system formed by $\{r_i; a_i, \beta_i, \gamma_i\}$ is denoted as $\mathrm{Fra}_{(i)}$, and the correlation vectors satisfy the Frenet formula:

$$ \dot{r} = a, \dot{a} = K\beta, \dot{\beta} = -Ka + \tau\gamma, \dot{\gamma} = -\tau\beta \quad (10) $$

where K and τ represent the curvature and torsion respectively.

$O_{F(i)} - X_{F(i)} - Y_{F(i)} - Z_{F(i)}$ is the feed coordinate system at point $O_{F(i)}$, denoted as $\mathrm{FCS}_{(i)}$. It should be noted that the $X_{F(i)}$-axis completely coincides with vector a_i, and $Z_{F(i)}$-axis represents the tool-side unit normal vector of the DS at point $O_{F(i)}$. θ_i represents the angle that $Z_{F(i)}$-axis rotates around vector a_i to vector γ_i.The description method at point $O_{F(i+1)}$ is similar to the above.

Therefore, from point $O_{F(i)}$ to $O_{F(i+1)}$, the change of the feed coordinate system can be described as:

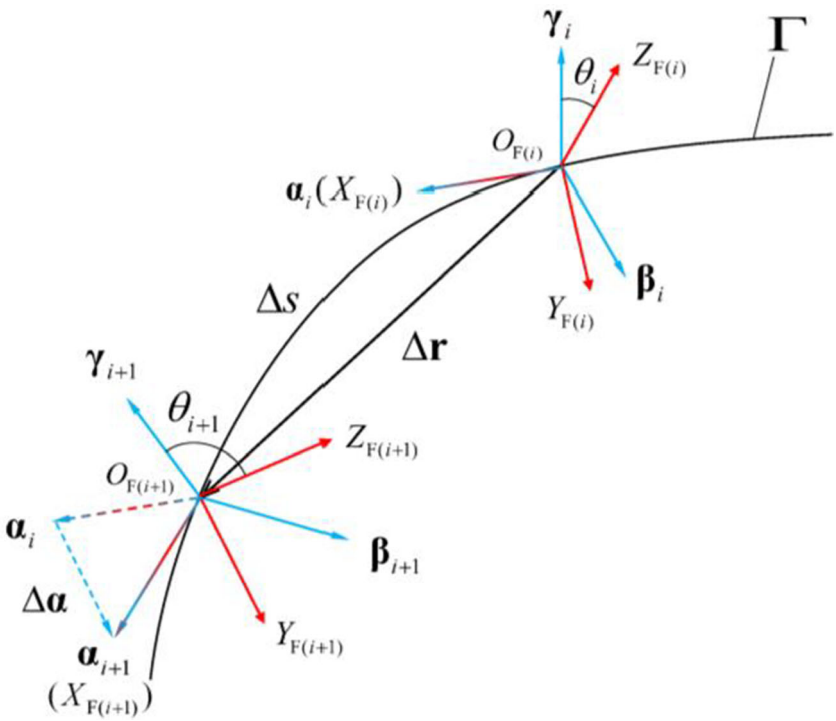

Fig. 5 Coordinate systems on tool path Γ

$$ {}^{\mathrm{FCS}_{(i)}}_{\mathrm{FCS}_{(i+1)}}\boldsymbol{T} = {}^{\mathrm{FCS}_{(i)}}_{\mathrm{Fra}_{(i)}}\boldsymbol{T}\,{}^{\mathrm{Fra}_{(i)}}_{\mathrm{Fra}_{(i+1)}}\boldsymbol{T}\,{}^{\mathrm{Fra}_{(i+1)}}_{\mathrm{FCS}_{(i+1)}}\boldsymbol{T} \tag{11} $$

where ${}^{\mathrm{FCS}_{(i)}}_{\mathrm{Fra}_{(i)}}\boldsymbol{T}$ and ${}^{\mathrm{Fra}_{(i+1)}}_{\mathrm{FCS}_{(i+1)}}\boldsymbol{T}$ are both simple rotation transformations and can be expressed as:

$$ {}^{\mathrm{FCS}_{(i)}}_{\mathrm{Fra}_{(i)}}\boldsymbol{T} = \begin{bmatrix} \boldsymbol{R}_x(\theta_i) & \boldsymbol{0} \\ \boldsymbol{0} & 1 \end{bmatrix}, \quad {}^{\mathrm{Fra}_{(i+1)}}_{\mathrm{FCS}_{(i+1)}}\boldsymbol{T} = \begin{bmatrix} \boldsymbol{R}_x(-\theta_{i+1}) & \boldsymbol{0} \\ \boldsymbol{0} & 1 \end{bmatrix} \tag{12} $$

where:

$$ \mathbf{R}_x(\theta) = \begin{bmatrix} 1 & 0 & 0 \\ 0 & \cos\theta & -\sin\theta \\ 0 & \sin\theta & \cos\theta \end{bmatrix} \tag{13} $$

Combined with the Frenet formula, the Taylor expansion of tool path Γ at point $O_{\mathrm{F}(i)}$ can be expressed as:

$$ \Delta\boldsymbol{r} = \boldsymbol{r}_{i+1} - \boldsymbol{r}_1 = \boldsymbol{a}_i\Delta s + \frac{K_i}{2}\boldsymbol{\beta}_i\Delta s^2 + o\left(\Delta s^3\right) \tag{14} $$

$$ \Delta\boldsymbol{a} = \boldsymbol{a}_{i+1} - \boldsymbol{a}_i = K_i\boldsymbol{\beta}_i\Delta s + \frac{-K_i^2\boldsymbol{a}_i + \dot{K}_i\boldsymbol{\beta}_i + K_i\boldsymbol{\tau}_i\gamma_i}{2}\Delta s^2 + o\left(\Delta s^3\right) \tag{15} $$

$$ \Delta\boldsymbol{\beta} = \boldsymbol{\beta}_{i+1} - \boldsymbol{\beta}_i = (-K_i\boldsymbol{\alpha}_i + \tau_i\boldsymbol{\gamma}_i)\Delta s + \frac{-\dot{K}_i\boldsymbol{\alpha}_i - (K_i^2 + \tau_i^2)\boldsymbol{\beta}_i + \dot{\tau}_i\boldsymbol{\gamma}_i}{2}\Delta s^2 + o\left(\Delta s^3\right) \tag{16} $$

$$ \Delta\boldsymbol{\gamma} = \boldsymbol{\gamma}_{i+1} - \boldsymbol{\gamma}_i = -\boldsymbol{\tau}_i\boldsymbol{\beta}_i\Delta s + \frac{K_i\boldsymbol{\tau}_i\boldsymbol{a}_i + \dot{\boldsymbol{\tau}}_i\boldsymbol{\beta}_i - \boldsymbol{\tau}_i^2\boldsymbol{\gamma}_i}{2}\Delta s^2 + o\left(\Delta s^3\right) \tag{17} $$

Equations (14)–(17) can be rewritten as:

$$ \begin{bmatrix} \boldsymbol{\alpha}_i \\ \boldsymbol{\beta}_i \\ \boldsymbol{\gamma}_i \end{bmatrix}^{\mathrm{T}} \begin{bmatrix} a_{11}-1 & a_{12} & a_{13} & a_{14} \\ a_{21} & a_{22}-1 & a_{23} & a_{24} \\ a_{31} & a_{32} & a_{33}-1 & a_{34} \end{bmatrix} = \begin{bmatrix} \Delta\boldsymbol{\alpha} & \Delta\boldsymbol{\beta} & \Delta\boldsymbol{\gamma} & \Delta\mathbf{r} \end{bmatrix} \tag{18} $$

where a_{**} is the expression containing parameters such as K_i, τ_i, and Δs. According to the definition of homogeneous transformation matrix, ${}^{\mathrm{Fra}_{(i)}}_{\mathrm{Fra}_{(i+1)}}\boldsymbol{T}$ can be expressed as:

$$ {}^{\mathrm{Fra}_{(i)}}_{\mathrm{Fra}_{(i+1)}}\boldsymbol{T} = \begin{bmatrix} a_{11} & a_{12} & a_{13} & a_{14} \\ a_{21} & a_{22} & a_{23} & a_{24} \\ a_{31} & a_{32} & a_{33} & a_{34} \\ 0 & 0 & 0 & 1 \end{bmatrix} \tag{19} $$

After the above, ${}^{\mathrm{FCS}_{(i)}}_{\mathrm{FCS}_{(i+1)}}\boldsymbol{T}$ is obtained. In order to express the cutter feed motion in the form of screw, it is necessary to analyze its influence on the instantaneous velocity of cutting edge elements. Suppose that point Q_i is a certain cutting edge element, whose coordinate in $\mathrm{FCS}_{(i)}$ is $(x_{\mathrm{F}}, y_{\mathrm{F}}, z_{\mathrm{F}}, 1)$. When the feed coordinate system moves to $\mathrm{FCS}_{(i+1)}$, point Q_i moves to point Q_{i+1}, as shown in Fig. 6 (it can be found that the moving distance of point Q_i is affected by the curvature), and they satisfy the following expressions:

$$ Q_i^{(\mathrm{FCS}_{(i)})} = Q_{i+1}^{(\mathrm{FCS}_{(i+1)})} = \begin{bmatrix} x_{\mathrm{F}} & y_{\mathrm{F}} & z_{\mathrm{F}} & 1 \end{bmatrix}^{\mathrm{T}} \tag{20} $$

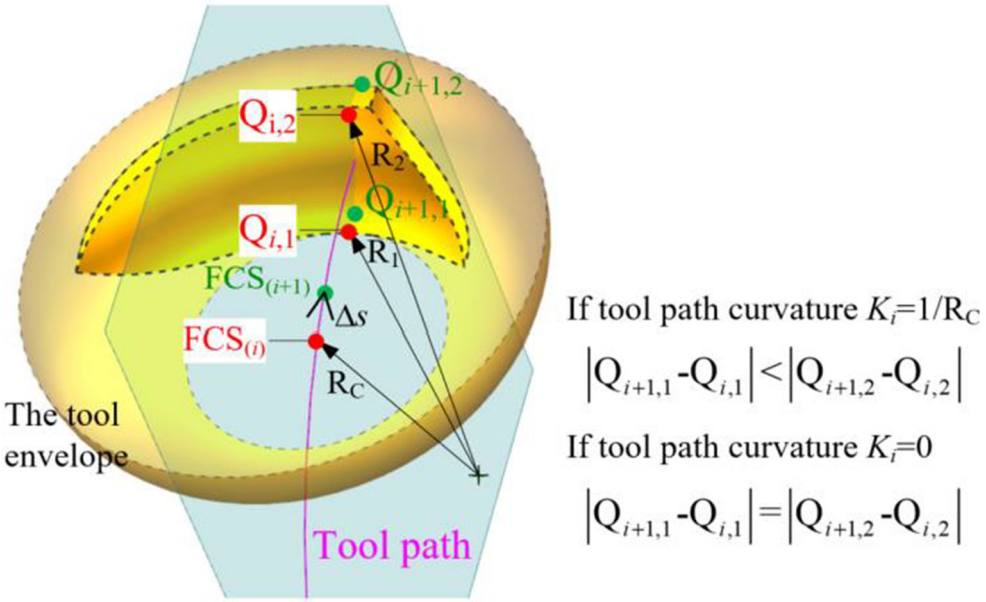

Fig. 6 The motion model of cutting edge elements induced by the feed motion considering the tool path curvature

The displacement from point Q_i to point Q_{i+1} can be expressed in $FCS_{(i)}$ as:

$$[\Delta x_1 \ \ \Delta y_1 \ \ \Delta z_1 \ \ 0]^{T(FCS_{(i)})} = {}^{FCS_{(i)}}_{FCS_{(i+1)}}\boldsymbol{TQ}_{i+1}^{(FCS_{(i+1)})} - Q_i^{(FCS_{(1)})} \tag{21}$$

Suppose that the time when the cutter moves to $FCS_{(i)}$ and $FCS_{(i+1)}$ is t_i and t_{i+1}, respectively, and $t_{i+1} = t_i + \Delta t$, then the instantaneous velocity of point Q_i at t_i can be expressed as:

$$\begin{aligned}&[\,v_{x1} \quad v_{y1} \quad v_{z1}\,]^{T(FCS_{(i)})}\\ &= \lim_{\Delta s \to 0}[\,\Delta x_1 \quad \Delta y_1 \quad \Delta z_1\,]^{T(FCS_{(i)})} \cdot v_f/\Delta s\end{aligned} \tag{22}$$

where v_f is the tool feed rate, which satisfies $\Delta s = v_f \Delta t$. Combined with Eqs. (19)–(21), Eq. (22) can be transformed into the following form:

$$\begin{bmatrix} v_{x1} \\ v_{y1} \\ v_{z1} \end{bmatrix}^{(FCS_{(i)})} = v_f \cdot \begin{bmatrix} 0 & -K_i\cos\theta_i & -K_i\sin\theta_i & 1 \\ K_i\cos\theta_i & 0 & \dfrac{\dot{\theta}_i}{v_f} - \tau_i & 0 \\ K_i\sin\theta_i & \dfrac{-\dot{\theta}_i}{v_f} + \tau_i & 0 & 0 \end{bmatrix} \begin{bmatrix} x_F \\ y_F \\ z_F \\ 1 \end{bmatrix} \tag{23}$$

where the symbols with subscript i represent the value of the corresponding variable at time t_i.

2.2.2 Cutter-orientation change modeling

Since the analysis in this section is about the cutter-orientation change, the feed motion is not considered. Therefore, it is necessary to fix the feed coordinate system, and then consider the motion of cutting edge elements when the tool coordinate system moves from $TCS_{(i)}$ to $TCS_{(i+1)}$. Similarly, taking the cutting edge element Q_i as the analysis object, its coordinate in FCS is $(x_F, y_F, z_F, 1)$. After the cutter-orientation changes, point Q_i moves to point Q_{i+1}, as shown in Fig. 7, and their coordinates in the respective tool coordinate system remain unchanged, i.e., $Q_i^{(TCS_{(i)})} = Q_{i+1}^{(TCS_{(i+1)})}$. The displacement from point Q_i to point Q_{i+1} can be expressed in FCS as:

$$\begin{aligned}&[\Delta x_2 \ \ \Delta y_2 \ \ \Delta z_2 \ \ 0]^{T(FCS)} = Q_{i+1}^{(FCS)} - Q_i^{(FCS)}\\ &= \left({}^{FCS}_{TCS_{(i+1)}}\boldsymbol{T} - {}^{FCS}_{TCS_{(i)}}\boldsymbol{T}\right){}^{TCS(i)}_{FCS}\boldsymbol{TQ}_i^{(FCS)}\end{aligned} \tag{24}$$

where ${}^{FCS}_{TCS_{(i+1)}}\boldsymbol{T}$ and ${}^{FCS}_{TCS_{(i)}}\boldsymbol{T}$ can be obtained from Eq. (8). The instantaneous velocity of point Q_i can be derived by taking the derivative of Eq. (24) with respect to time t.

$$[v_{x2} \quad v_{y2} \quad v_{z2} \quad 0]^{T(FCS)} = \left.\frac{d\left({}^{FCS}_{TCS}\boldsymbol{T}\right)}{dt}\right|_{t=t_i} {}^{TCS_{(i)}}_{FCS}\boldsymbol{T}[x_F \quad y_F \quad z_F \quad 1]^T \tag{25}$$

The above formula can be further reduced to the following form:

$$\begin{bmatrix} v_{x2} \\ v_{y2} \\ v_{z2} \end{bmatrix}^{(FCS)} = \begin{bmatrix} 0 & -\dot{l}sT & -\dot{l}cT & A\dot{l} + B\dot{t} \\ \dot{l}sT & 0 & -\dot{t} & C\dot{l} + E\dot{t} \\ -\dot{l}cT & \dot{t} & 0 & F\dot{l} + G\dot{t} \end{bmatrix} \begin{bmatrix} x_F \\ y_F \\ z_F \\ 1 \end{bmatrix} \tag{26}$$

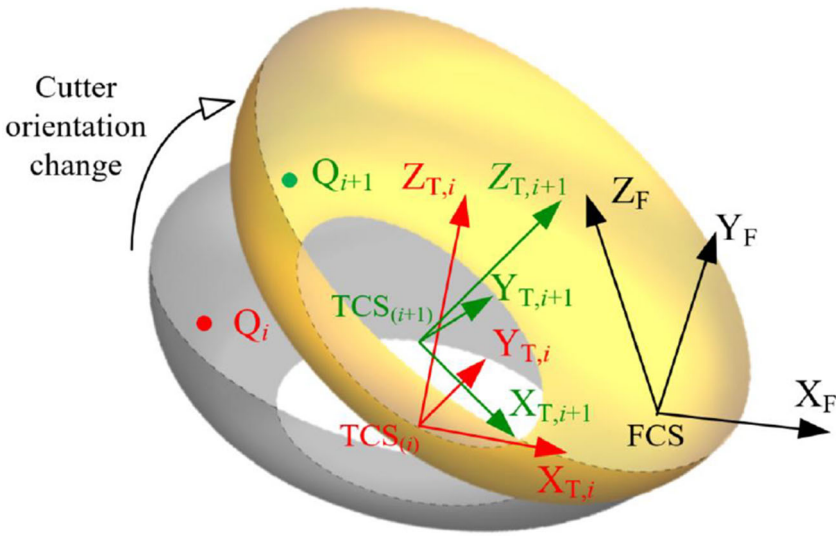

Fig. 7 The motion model of cutting edge elements induced by the cutter-orientation change

where:

$$
\begin{aligned}
A &= -rcl(c\kappa_i - 1) - r_i s\varphi_i sl \\
B &= 0 \\
C &= r_i s\varphi_i clst - r(c\kappa_i - 1)slst \\
E &= r_i s\varphi_i slct + r(c\kappa_i - 1)clct - r_i c\varphi_i st \\
F &= -r_i s\varphi_i clct + r(c\kappa_i - 1)slct \\
G &= r_i s\varphi_i slst + r(c\kappa_i - 1)clst + r_i c\varphi_i ct
\end{aligned}
$$

where s is sin, c is cos, l is $lead_i$, and t is $tilt_i$ when used after s or c. $lead_i$ and $tilt_i$ represent the lead angle and the tilt angle at time t_i, respectively. $\dot{i}$ and $\dot{t}$ represent their rate of change. r_i, φ_i, and k_i represent the effective cutting radius, radial location angle, and axial contact angle of the cutter contact point at time t_i, respectively.

2.2.3 Screw modeling

The above two sections have analyzed the motion of the cutting edge element Q_i caused by the feed motion and the cutter-orientation change respectively. On this basis, the screw expression of the cutter composite motion is derived below.

The screw representing the cutter spatial motion in FCS is denoted as $[V_\mathrm{F}] = (\mathbf{v}_\mathrm{F}, \boldsymbol{\omega}_\mathrm{F})$, and it satisfies $\mathbf{v}_\mathrm{F} = \mathbf{r}_\mathrm{F} \times \boldsymbol{\omega}_\mathrm{F} + h_\mathrm{F}\boldsymbol{\omega}_\mathrm{F}$, where $\boldsymbol{\omega}_\mathrm{F} = [\omega_{\mathrm{F}x} \quad \omega_{\mathrm{F}y} \quad \omega_{\mathrm{F}z}]^\mathrm{T}$ is the angular velocity, h_F is the pitch, $\mathbf{r}_\mathrm{F} = [r_{\mathrm{F}x} \quad r_{\mathrm{F}y} \quad r_{\mathrm{F}z}]^\mathrm{T}$ is the orthogonal position vector and satisfies $\boldsymbol{\omega}_\mathrm{F} \perp \mathbf{r}_\mathrm{F}$:

$$\omega_{\mathrm{F}x} r_{\mathrm{F}x} + \omega_{\mathrm{F}y} r_{\mathrm{F}y} + \omega_{\mathrm{F}z} r_{\mathrm{F}z} = 0 \tag{27}$$

Then the instantaneous velocity of point $Q_i(x_\mathrm{F}, y_\mathrm{F}, z_\mathrm{F})$ under the action of screw $[V_\mathrm{F}]$ can be expressed as:

$$
\begin{bmatrix} v_x \\ v_y \\ v_z \end{bmatrix}^{(\mathrm{FCS})} = (r_\mathrm{F} - Q_i) \times \omega_\mathrm{F} + h_\mathrm{F}\omega_\mathrm{F} = \begin{bmatrix} 0 & -\omega_{\mathrm{F}z} & \omega_{\mathrm{F}y} & h_\mathrm{F}\omega_{\mathrm{F}x} - r_{\mathrm{F}z}\omega_{\mathrm{F}y} + r_{\mathrm{F}y}\omega_{\mathrm{F}z} \\ \omega_{\mathrm{F}z} & 0 & -\omega_{\mathrm{F}x} & r_{\mathrm{F}z}\omega_{\mathrm{F}x} + h_\mathrm{F}\omega_{\mathrm{F}y} - r_{\mathrm{F}x}\omega_{\mathrm{F}z} \\ -\omega_{\mathrm{F}y} & \omega_{\mathrm{F}x} & 0 & -r_{\mathrm{F}y}\omega_{\mathrm{F}x} + r_{\mathrm{F}x}\omega_{\mathrm{F}y} + h_\mathrm{F}\omega_{\mathrm{F}z} \end{bmatrix} \begin{bmatrix} x_\mathrm{F} \\ y_\mathrm{F} \\ z_\mathrm{F} \\ 1 \end{bmatrix} \tag{28}
$$

$[V_\mathrm{F}]$ can be solved by combining Eq. (28) and the following equation:

$$
\begin{aligned}
[v_x \quad v_y \quad v_z]^{\mathrm{T(FCS)}} = {} & [v_{x1} \quad v_{y1} \quad v_{z1}]^{\mathrm{T}\left(\mathrm{FCS}_{(i)}\right)} \\
& + [v_{x2} \quad v_{y2} \quad v_{z2}]^{\mathrm{T(FCS)}}
\end{aligned} \tag{29}
$$

where the formulas on the right side can be obtained by Eqs. (23) and (26) respectively. It should be noted that the above formula is unsolvable when $\omega_{\mathrm{F}x} = \omega_{\mathrm{F}y} = \omega_{\mathrm{F}z} = 0$, namely, when the tool is in translation, then $[V_\mathrm{F}] = (\mathbf{v}_\mathrm{F}, 0)$ and $\mathbf{v}_\mathrm{F} = \left[A\dot{l} + B\dot{t} + v_f C\dot{l} + Dt\dot{E}l + F\dot{t}\right]^\mathrm{T}$.

The screw representing the cutter spatial motion in TCS is denoted as $[V_\mathrm{T}] = (\mathbf{v}_\mathrm{T}, \boldsymbol{\omega}_\mathrm{T})$, whose orthogonal position vector is $\mathbf{r}_\mathrm{T}$ and pitch is h_T. Then, $[V_\mathrm{T}]$ and $[V_\mathrm{F}]$ satisfy:

$$\boldsymbol{\omega}_\mathrm{T} = {}^{\mathrm{TCS}}_{\mathrm{FCS}}\mathbf{R}\boldsymbol{\omega}_\mathrm{F}, \quad \begin{bmatrix} \mathbf{r}_\mathrm{T} \\ 1 \end{bmatrix} = {}^{\mathrm{TCS}}_{\mathrm{FCS}}\mathbf{T}\begin{bmatrix} \mathbf{r}_\mathrm{F} \\ 1 \end{bmatrix}, \quad h_\mathrm{T} = h_\mathrm{F} \tag{30}$$

$[V_\mathrm{T}] = (\mathbf{v}_\mathrm{T}, 0)$ when the tool is in translation, where $\mathbf{v}_\mathrm{T} = {}^{\mathrm{TCS}}_{\mathrm{FCS}}\mathbf{R}\mathbf{v}_\mathrm{F}$.

The screw obtained in this section can accurately represent the instantaneous motion of each cutting edge element at time t_i. In the simulation, Δt and Δs are so small that it can be considered that the motion state of the cutter has not changed within $t_i \sim t_{i+1}$, so there is basically no interpolation error when calculating the IUCT and the cutter envelope surface by the screw.

3 Cutting force modeling based on screw

3.1 IUCT calculating

The solution method of IUCT used in this paper is vector projection method based on motion screw. Because the modeling of motion screw takes into account the influence of curvature and torsion of tool path and the change of cutter orientation, the precision of IUCT is also improved accordingly. In the simulation analysis, the change of relevant parameters can be easily controlled to study the influence of the tool path curvature and torsion, and the change of the cutter orientation on the lump IUCT under specific working conditions.

The screw in TCS (i.e., $[V_\mathrm{T}]$) has been obtained in Section 2.2.3 (if there is no special mark, all the following vectors and coordinates are based on TCS). Suppose that point Q, denoting any cutting edge element, moves to point Q_s after time t under the action of $[V_\mathrm{T}]$, then the coordinates of Q_s can be drawn in Fig. 8 and expressed as:

$$Q_s = (\theta\boldsymbol{\omega}_1) \otimes \mathbf{R}_P + \mathbf{r}_\mathrm{T} + h_\mathrm{T}\boldsymbol{\omega}_\mathrm{T}t \tag{31}$$

where $(\theta\omega_i) \otimes R_p$ represents the rotation of R_p around ω_i by θ, $\boldsymbol{\omega}_1 = [\omega_{1x} \quad \omega_{1y} \quad \omega_{1z}]^\mathrm{T} = \boldsymbol{\omega}_\mathrm{T}/|\boldsymbol{\omega}_\mathrm{T}|$, $\mathbf{R}_P = [R_x \quad R_y \quad R_z]^\mathrm{T} = Q - \mathbf{r}_\mathrm{T}$, $\theta = |\boldsymbol{\omega}_\mathrm{T}|t$, and the coordinates of point Q_s can be obtained from Eq. (1). Then, Eq. (31) can be transformed into:

$$Q_s = \begin{bmatrix} r_{Tx} + R_x c\theta + (\omega_{1y}R_z - \omega_{1z}R_y)s\theta + (1-c\theta)(\omega_{1x}R_x + \omega_{1y}R_y + \omega_{1z}R_z)\omega_{1x} + h_T\omega_{Tx}t \\ r_{Ty} + R_y c\theta + (\omega_{1z}R_x - \omega_{1x}R_z)s\theta + (1-c\theta)(\omega_{1x}R_x + \omega_{1y}R_y + \omega_{1z}R_z)\omega_{1y} + h_T\omega_{Ty}t \\ r_{Tz} + R_z c\theta + (\omega_{1x}R_y - \omega_{1y}R_x)s\theta + (1-c\theta)(\omega_{1x}R_x + \omega_{1y}R_y + \omega_{1z}R_z)\omega_{1z} + h_T\omega_{Tz}t \end{bmatrix} \quad (32)$$

where s is sin, c is cos.

As shown in Fig. 9, expressing the displacement of cutting edge element Q_s in a tooth passing period Δt as $\Delta Q = Q_s|_{t-\Delta t} - Q$, the IUCT of Q_s can be expressed as [7]:

$$h_Q = \Delta Q \cdot n_Q \quad (33)$$

where n_Q represents the outer unit normal vector of the tool surface at point Q, which can be obtained by Eq. (6). In addition, $Q_s = Q + \mathbf{v}_T t$, $h_Q = \mathbf{v}_T \Delta t \cdot \mathbf{n}_Q$ when the tool is in translation.

3.2 Cutting state judgment of cutting edge elements

As shown in Fig. 10, Zhu et al. [17] divided CWE boundary curves into three curves: the intersection curve, the projective curve, and the characteristic curve, where the projective curve is the intersection curve of the current tool surface and the previous tool path forming surface, so only the characteristic curve is affected by the current motion state of the cutting edge elements. Gong et al. [32] pointed out that the grazing points constituting the characteristic curve satisfy $v \cdot n = 0$, where v is the instantaneous velocity of the grazing points, and n is the outer unit normal vectors of the tool surface at the grazing points. Meanwhile, since the instantaneous velocity of a grazing point is parallel to its feed vector, combining with the definition of the vector projection method [7], it can be seen that $v \cdot n = 0$ is equivalent to $IUCT = 0$, this is to say the characteristic curve can also be solved by $IUCT = 0$. Hence, the influence of the tool path curvature and torsion, and cutter-orientation change on CWE can be regarded as the result of their influence on IUCT. For this reason, this paper does not directly establish the CWE model, but determines the cutting state of the cutting edge elements based on their IUCT and position relative to the workpiece surface, which is similar to the method in references [7, 10, 12]. And the difference is that the IUCT model in this paper takes into account the tool path curvature and torsion, and cutter-orientation change, so the accuracy of judging the cutting state of the cutting edge elements is improved compared with references [7, 10, 12].

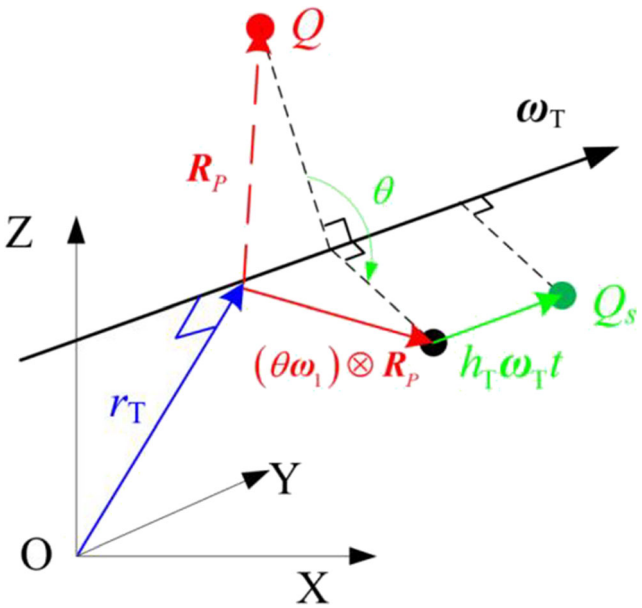

Fig. 8 The lump screw motion model of cutting edge element Q_s

The two conditions for judging that any cutting edge element Q participates in cutting are as follows:

1. The IUCT of Q is greater than 0, i.e. $h_Q > 0$.
2. Q must be below the workpiece surface. This comparison is carried out in WCS, where the coordinates of Q in WCS can be obtained by combining Eqs. (1), (8), and (9), and the method for obtaining the coordinates of the workpiece surface at any position can be referred to in reference [12].

The cutting state of the cutting edge element Q is represented by the function $g(Q)$: when Q satisfies the above two conditions, $g(Q) = 1$; otherwise, $g(Q) = 0$.

The estimation of CWE is detected by the cutting edge element position one by one. The cutting edge element is in-cutting under the conditions of both the cutting edge element being below the workpiece surface and its IUCT being larger than 0. The two conditions are calculated with the cutter geometry model and the cutter motion model based on the screw theory. As the cutter motion model in this paper is not only suitable for spiral or other spatial curve tool paths but also suitable for three-axis or five-axis milling, the proposed method of judging CWE is suitable for the relevant strategies mentioned. In addition, the proposed method of judging CWE is also suitable for continuous cutting path by path, as the workpiece surface can be updated with the cutter envelope surface through the workpiece surface updating model in Section 3.3. However, the method to estimating CWE in this paper is not suitable for micro-milling for lack of accurate IUCT model when considering the cutting edge radius, rank angle, and other factors related to size effect.

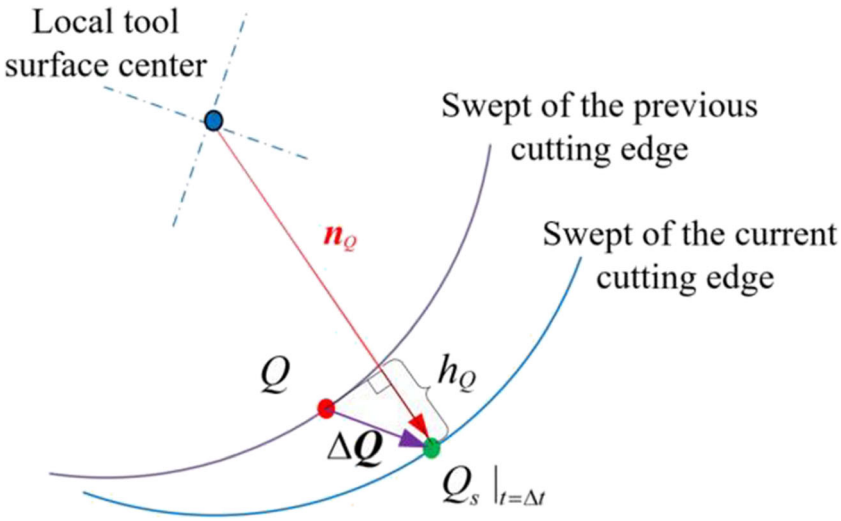

Fig. 9 Schematic diagram of IUCT

3.3 Workpiece surface updating

In the simulation of cutting with multiple adjacent tool paths, except for the first tool path, the subsequent tool paths need to update the workpiece surface according to the tool envelope surface of the previous tool path before their simulations to correctly judge the cutting state of cutting edge elements, as shown in Fig. 11. The specific method is as follows.

In the tool feed process, Q_s in Section 3.1 is essentially a single parametric surface family about time t, which can be expressed as $Q_s = Q_s(z, \varphi, t)$. Then, the cutter envelope surface under the action of the screw can be determined by the following formula [33]:

$$\left(\frac{\partial Q_s}{\partial z}, \frac{\partial Q_s}{\partial \varphi}, \frac{\partial Q_s}{\partial t}\right) = 0 \tag{34}$$

By taking $t \in [t_i, t_{i+1}]$, the cutter envelope surface in the time period $t_i \sim t_{i+1}$ can be obtained from the above equation, which can be discretized into the point cluster $\Pi_i^{(\mathrm{TCS}_{(i)})}$ by using Eq. (1). Then, $\Pi_i^{(\mathrm{TCS}_{(i)})}$ can be converted into WCS:

$$\Pi_i^{(\mathrm{WCS})} = {}^{\mathrm{WCS}}_{\mathrm{FCS}_{(i)}}\mathbf{T}\left({}^{\mathrm{TCS}_{(i)}}_{\mathrm{FCS}_{(i)}}\mathbf{T}\right)^{-1}\Pi_i^{(\mathrm{TCS}_{(i)})} \tag{35}$$

where ${}^{\mathrm{TCS}_{(i)}}_{\mathrm{FCS}_{(i)}}\mathbf{T}$ and ${}^{\mathrm{WCS}}_{\mathrm{FCS}_{(i)}}\mathbf{T}$ can be obtained from Eq. (8) and (9), respectively. By combining the point clusters of the cutter envelope surface of each time period in a tool path, the cutter envelope surface of the entire tool path can be obtained, and its expression is $\Pi^{(\mathrm{WCS})} = \sum_i \Pi_i^{(\mathrm{WCS})}$. After that, the workpiece surface can be updated by Boolean subtraction operation between the cutter envelope surface and the workpiece surface, and the specific method of Boolean operation can be referred to in reference [12].

3.4 Cutting force model

In Fig. 2, dF_t, dF_r, and dF_a are the tangential, radial, and axial chip load of the cutting edge element Q, respectively,

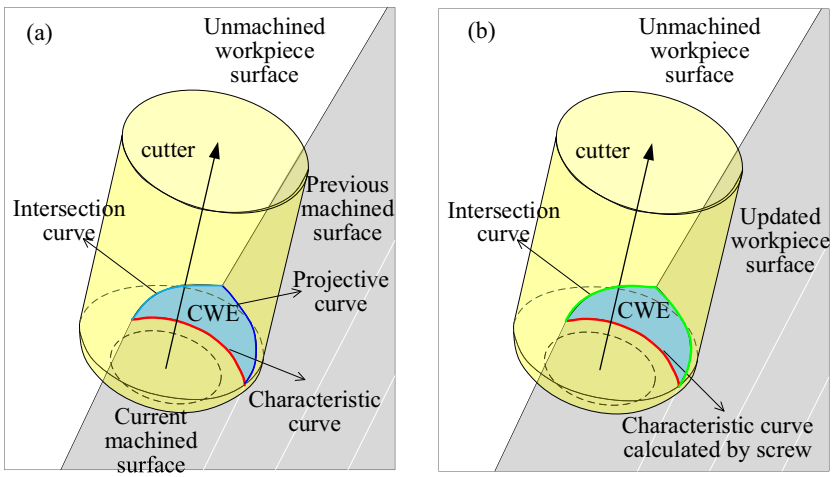

Fig. 10 The cutting state judgment of cutting edge element (a) method in [17] and (b) method in this paper

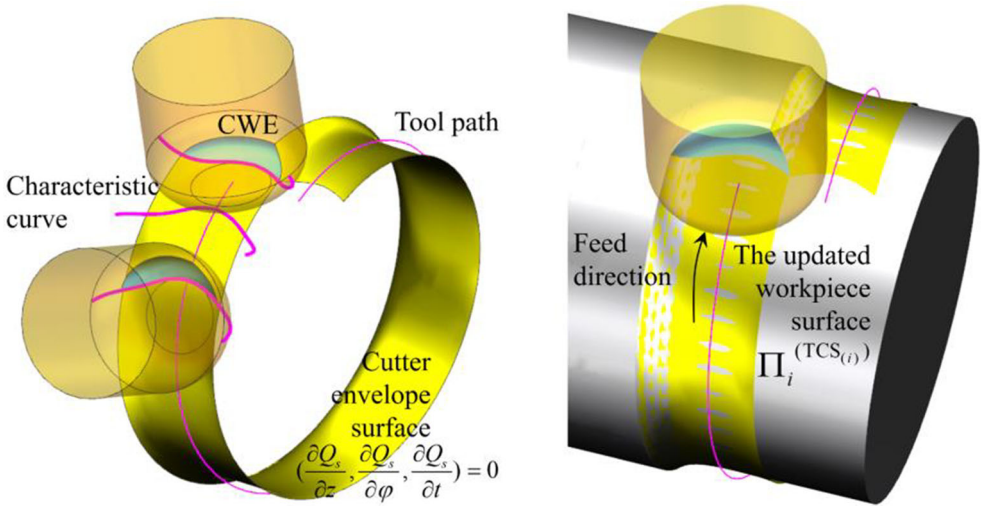

Fig. 11 The cutter envelope surface and the updated workpiece surface

satisfying the following expression:

$$\begin{bmatrix} dF_t \\ dF_r \\ dF_a \end{bmatrix} = \begin{bmatrix} g(Q)K_t h_Q d_z/\sin\kappa \\ g(Q)K_r h_Q d_z/\sin\kappa \\ g(Q)K_a h_Q d_z/\sin\kappa \end{bmatrix} \tag{36}$$

where K_t, K_r, and K_a respectively represent the cutting force coefficients in the corresponding direction, d_z represents the height of each discrete disk in the tool axis and $d_z = H/H_z$, and N_z is the number of the disks. $h_{\underline{o}}$ and $g(Q)$ can be obtained from Sections 3.1 and 3.2 respectively.

Convert the chip loads of Q to TCS:

$$\begin{bmatrix} dF_x \\ dF_y \\ dF_z \end{bmatrix} = \begin{bmatrix} -\cos\varphi & -\sin\kappa\sin\varphi & -\cos\kappa\sin\varphi \\ \sin\varphi & -\sin\kappa\cos\varphi & -\cos\kappa\cos\varphi \\ 0 & \cos\kappa & -\sin\kappa \end{bmatrix} \begin{bmatrix} dF_t \\ dF_r \\ dF_a \end{bmatrix} \tag{37}$$

Then, the instantaneous milling force is the sum of the chip loads of all cutting edge elements:

$$\begin{bmatrix} F_x \\ F_y \\ F_z \end{bmatrix} = \sum_{j_c=1}^{N} \sum_{i=1}^{N_z} \begin{bmatrix} dF_x \\ dF_y \\ dF_z \end{bmatrix} \tag{38}$$

where i is the serial number of the discrete disk.

4 Algorithm flow chart of cutting force simulation

Figure 12 is the flow chart of cutting force simulation, which is mainly divided into three parts: tool motion modeling, cutting force predicting, and workpiece surface updating. Firstly, the first cutting point of the first tool path is simulated. According to the motion screw model in Section 2, the workpiece surface, tool path, tool parameters, and machining parameters are used to model the tool motion screw at this cutting point. Then, according to the method in Sections 3.1 and 3.2 respectively, the IUCT of the cutting edge element between the current cutting point and the next cutting point is solved and the cutting state is judged. Then, according to the cutting force model in Section 3.4, the cutting force between the two cutting points can be obtained. Then, the cutting force of the whole cutting path can be simulated by changing the cutter site in turn. In addition, considering that the tool path of sculptured surface machining is composed of several continuous or discontinuous local parallel tool path, the material removal in the current machining is based on the previous adjacent tool path. After the cutting force simulation of the previous tool path is completed, the envelope surface and workpiece surface between all cutting points of the previous tool path should be collected, and the workpiece surface should be updated by Boolean deduction operation (Section 3.3). Then, the cutting force simulation of the next cutter path should be carried out in turn until the milling is completed.

5 Experimental verification

5.1 Calibration of cutting force coefficients

Experiments and studies show that the milling force coefficient can be expressed as an exponential function of the instantaneous undeformed chip thickness [34], as shown in Eq. (39), which is independent of the milling mode and cutting parameters. Therefore, the milling force coefficients can be calibrated by using the milling force data of three-axis milling, and the obtained coefficients can be used to analyze and verify the milling force of five-axis milling.

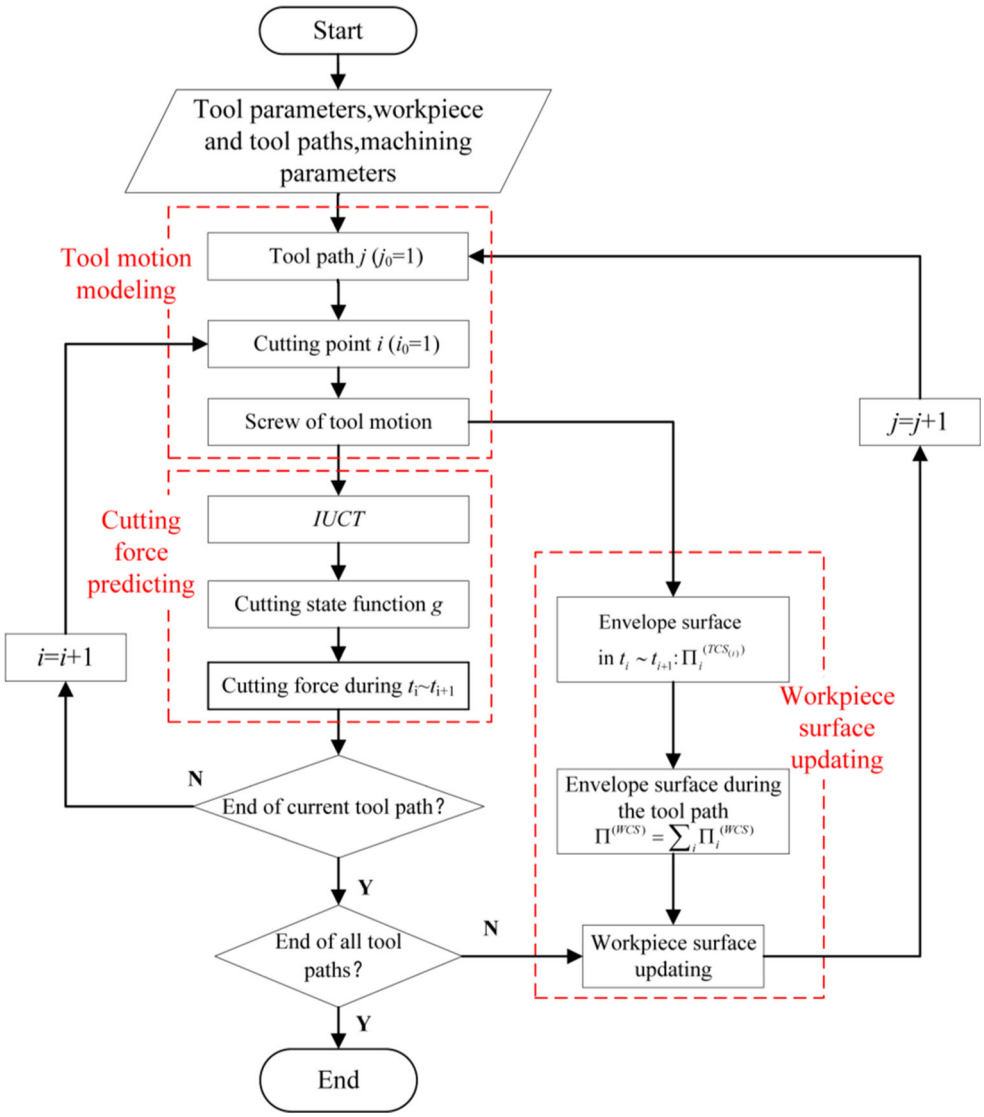

Fig. 12 Algorithm flow chart of cutting force simulation

$$K_{t,r,a} = \mathrm{A}_{t,r,a} + \mathrm{B}_{t,r,a} e^{-\mathrm{C}_{t,r,a} h_Q} \tag{39}$$

where, $\mathrm{A_{t,r,a}}$, $\mathrm{B_{t,r,a}}$, and $\mathrm{C_{t,r,a}}$ are constant coefficients, which are obtained by cutting experiment calibration. h_Q is IUCT, and can be expressed as $h_Q = f \sin\varphi \sin\kappa$ for three-axis machining with the feed rate f, radial position angle φ, and axial position angle κ.

During the force coefficients calibrating, h_Q denotes the average uncut chip thickness of all in-cutting cutting edge elements for a specific cutter rotation angle in these experimental equations. And combined with the measured instantaneous cutting force of the tool rotation angle, we can get the milling force coefficients related to the average undeformed chip thickness. It should be noted that the calibration method used here is based on the three-axis milling force model, and the method in [35] could be referred if the cutter runout and surface inclinations are hidden in the input instantaneous force signals.

The milling force coefficient identification experiment of TC4 with carbide end milling cutter was carried out in Mikron UCP800 machining center. Tool diameter D = 8 mm, fillet

Table 1 The cutter parameters and the machining parameters

Parameters	Values
Cutter type	Bullnose end cutter
Cutter diameter (mm)	8
Fillet radius (mm)	1
Number of the cutter flutes	2
Cutter helix angle (°)	30
Spindle speed (*r*/min)	1200
Feed per tooth (mm)	0.075
Rake angle (°)	17

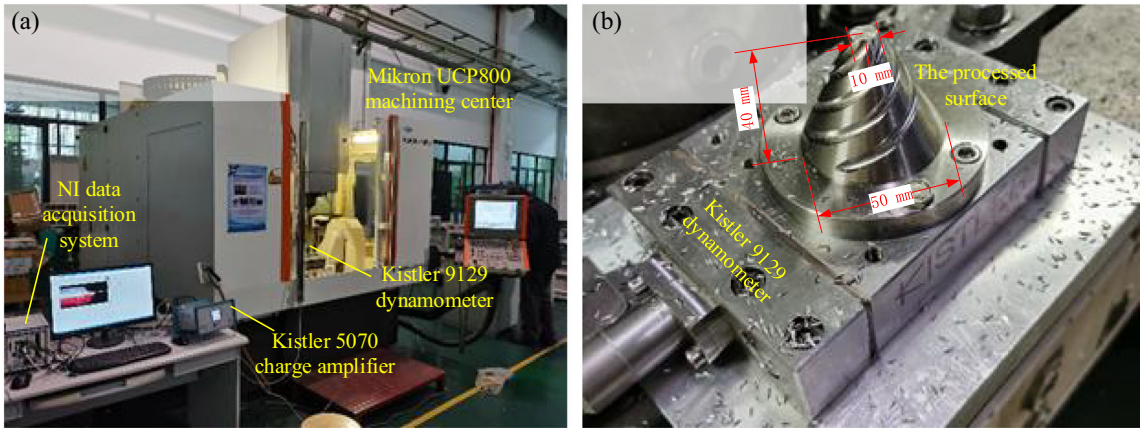

Fig. 13 Machining site and experimental equipment. (a) The machining site and the monitoring system of milling force (b) The workpiece features and the clamping

radius r = 1 mm, helical angle is 30° as shown in Table 1. Kistler 9129 piezoelectric dynamometer and Kistler 5070 charge amplifier were used to monitor the milling force during the cutting process. NI PXIe 4499 data acquisition card was used to collect and process the milling force data with a sampling frequency of 10 KHz. The identification results of milling force coefficient are shown in Table 2.

5.2 Model validation experiment

In order to verify the accuracy of the cutting force prediction model, milling experiments of TC4 were carried out in Mikron UCP800 machining center. The cutting tool used in the experiment was same as the milling force coefficient calibration experiment, which was a Sandvik carbide end mill and the cutter parameters are listed in Table 1. The machining site and the monitoring system of milling force are shown in Fig. 13(a). Kistler 9129 piezoelectric dynamometer and Kistler 5070 charge amplifier were used to monitor the milling force during the cutting process. NI PXIe4499 data acquisition card was used to collect and process the milling force data. The workpiece features and the clamping device of the dynamometer are shown in Fig. 13(b). The workpiece is a cone with top circle diameter of 10 mm, bottom circle diameter of 50 mm, and height of 40 mm.

In order to verify the milling force model considering the tool path curvature and torsion, and cutter-orientation change, the tool path of the verification experiment was a conical spiral attached to the conical surface, whose tangent vector direction, curvature, and torsion were all changing in different positions, and the lead and tilt angle of the cutter at different cutting points relative to the workpiece surface were also changing. In order to avoid interference or miscutting during cutting, the starting point of the tool path is 5 mm away from the cone bottom and the pitch is 10 mm. The helix angle of ergodic of the whole cutting path is π. During the cutting process, the tool is always vertical (that is, parallel to the axis of the cone), and groove milling is adopted. The cutting parameters adopted are the following: spindle speed 1200 r/min, cutting depth 1 mm, and feeding rate 3 mm/s.

Table 2 Milling force coefficient calibration results

Associated	A	B	C
K_t	424.5	302.1	38
K_r	1344.7	753.9	77
K_a	− 291.5	3775.2	130

Figure 14 shows the measured and simulated cutting forces on the whole tool path. Figure 14 (a) shows the milling force of the whole tool path, it can be seen that the experimental cutting forces in X, Y, Z directions respectively changed from − 230 N to 120 N, from − 210 N to 40, and from 40 N to 80 N, and the prediction errors in X direction and Y direction are below 10%. This is mainly due to the uncertainty factors in the processing process, such as tool vibration and material inhomogeneity. If the error caused by uncertain factors is ignored, the experimental results show that the prediction model of milling force is effective.

Figure 14 (b) shows the experimental value of milling force at 16 s after the tool cutting into the workpiece, and the comparison between the prediction results with the proposed method and the CEEM method without considering the tool path curvature and torsion, and cutter-orientation change in the literature [7]. It can be seen that the proposed model coincides almost completely with the experimental measurement values, which has higher prediction accuracy than CEEM method, while the result of method in [7] is generally small. In order to understand the influence mechanism of tool path curvature and torsion, and cutter-orientation change on milling force, the following section makes an in-depth analysis and discussion.

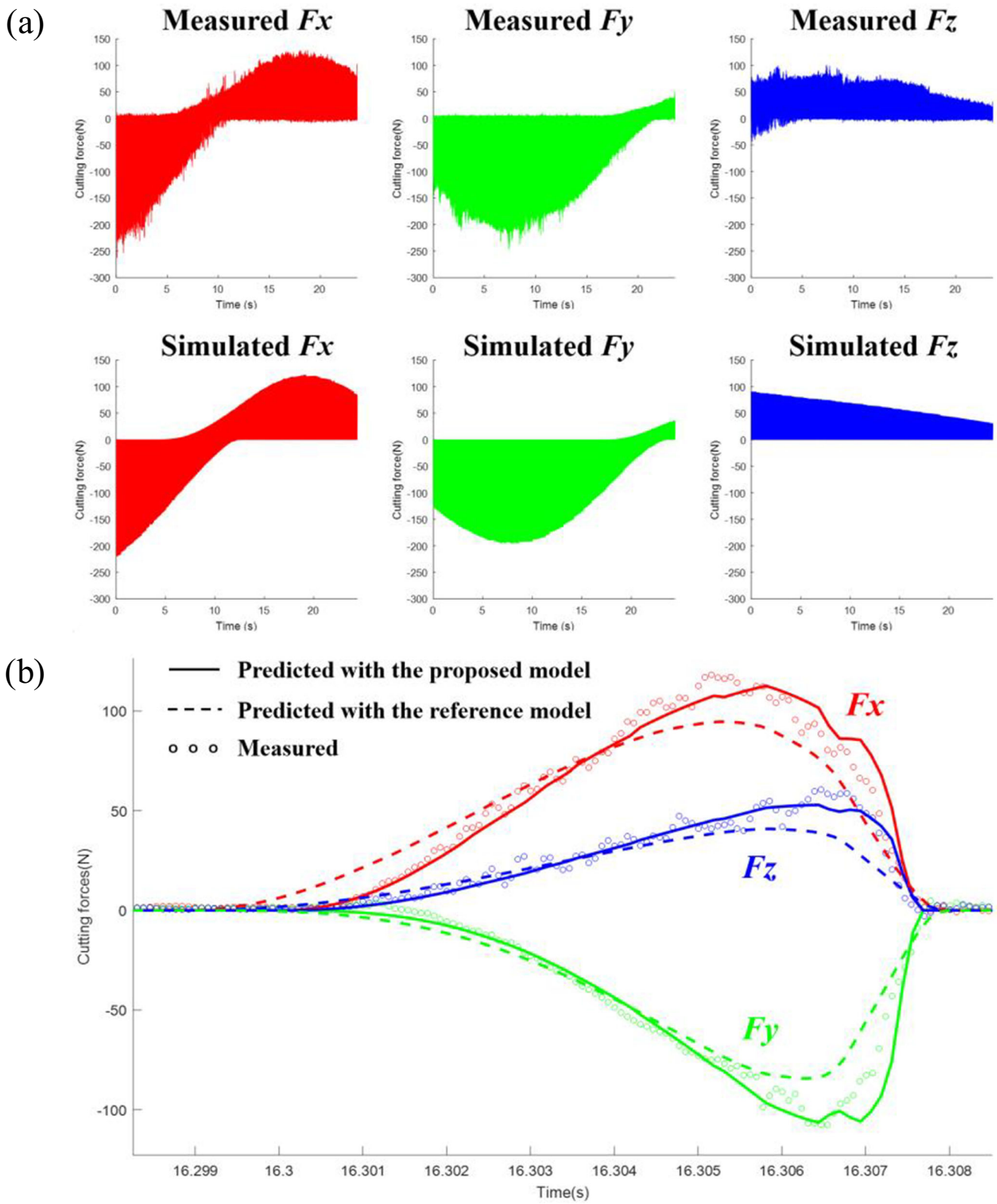

Fig. 14 Comparison of measured and simulated cutting forces (a) comparison of the whole helical cutting path (b) comparison of specific cutting moments

6 Simulations and discussions

In order to analyze the influence of the tool path curvature and torsion, and cutter-orientation change on cutting force, a cylindrical surface with similar shape to the leading and trailing edges of aero-engine blades is selected as the workpiece surface. The tool path is a cylindrical helix attached to the design surface, and the curvature (bending) and torsion equations of the helix are respectively

$$K = \frac{D/2-ap}{p^2 + (D/2-ap)^2} \tag{40}$$

$$\tau = \frac{p}{p^2 + (D/2-ap)^2} \tag{41}$$

where D is the diameter of the cylinder surface, ap is the cutting depth, ae is the cutting width, and P is the pitch. The edge features of a particular type of part are selected here, with the rounded corner diameter of 10 mm, and the cutting depth of 1 mm and cutting width of 2 mm are selected according to the cutting parameters of rough machining. Other parameters, such as spindle speed, feed rate, and cutting force coefficient, are consistent with the experiments in Section 5.

6.1 Influence of tool path curvature on cutting force

In order to analyze the influence of the curvature of the cutting path on the cutting force, set the pitch $p = 0$ for the cylindrical helical cutting path, then the curvature $K = 0.25$ by Eq. (40). According to Fig. 15, the prediction results of cutting forces with and without tool path curvature under different cutter orientations are compared. It can be seen that under different cutter orientations, the average cutting force with tool path curvature considered is increased compared with that without tool path curvature considered. The smaller the lead angle is and the larger the tilt angle is, the more the average cutting force increases. Figure 15 also shows the simulation curve of cutting force when the lead angle is 15° and the tilt angle is 45°. It can be seen that the tool path curvature has a significant influence on instantaneous cutting force.

Figure 16 is a schematic drawn with *lead* = 15° and *tilt* = 45°, where $O_{F(i+1)}'$ and $Z_{T(i+1)}'$ represent the cutter contact point and tool axis vector at time t_{i+1} without considering the tool path curvature, respectively, and the other symbols have the same meaning as in Section 2.2. It can be observed that under this cutter orientation, the tool path curvature increases the material removal.

According to Eq.s (23) and (28), $\omega_{Fy} = -K_i \sin\theta_i$ (where $\theta_i = -\pi/2$). Therefore, considering the tool path curvature K_i, ω_{Fy} increases. At this time, since $\mathbf{r}_F = [0 \quad 0 \quad -4]$, the orthogonal position vector $\mathbf{r}_F$ is located below the tool. Hence, the increase of ω_{Fy} enhances the tool motion in the feed direction, thereby increasing the IUCT, and resulting in the increase of the average cutting force. Further analysis shows that, regardless of the tool path curvature, the instantaneous velocity of each cutting edge element is the same as that of the cutter contact point. When considering the tool path curvature, the motion of each cutting edge element is considered separately. Moreover, the farther a cutting edge element is from the curvature center, the greater its instantaneous speed is, and the greater the corresponding IUCT increase.

6.2 Influence of tool path torsion on cutting force

In order to analyze the influence of the tool path torsion on the cutting force, the pitch is set as p = 4 mm, and

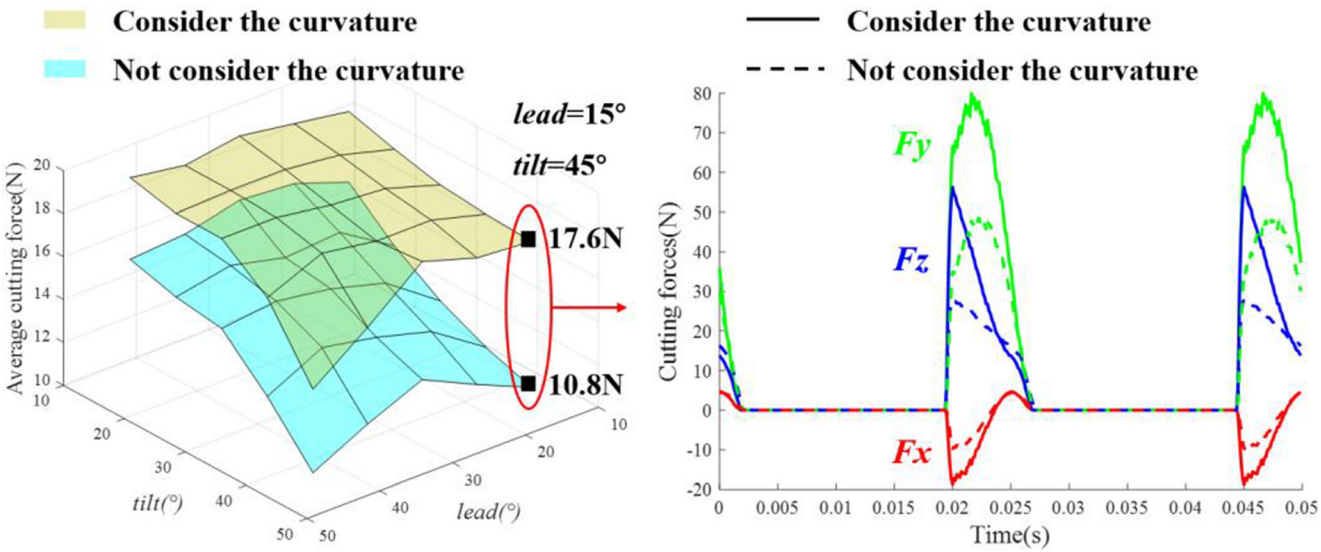

Fig. 15 Influence of the tool path curvature on cutting force

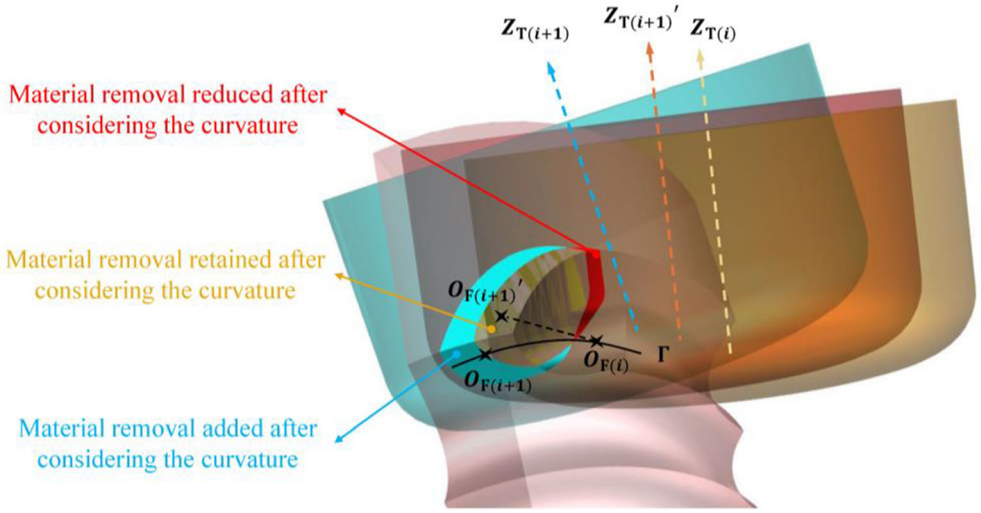

Fig. 16 Influence of the tool path curvature on cutting process

then the torsion is $\tau = 0.125$ according to Eq. (41). Figure 17 shows the comparison of the prediction effects of cutting forces with and without tool path torsion under different cutter orientations. It can be seen that under different cutter orientations, the average cutting forces with tool path torsion taken into account are larger compared with those without tool path path torsion. And the larger the lead angle is and the smaller the tilt angle is, the more the average cutting force increases. Figure 17 also shows the simulation curve of cutting force when the lead angle is 30° and the tilt angle is 15°. It can be seen that the influence of the tool path torsion on the instantaneous cutting force is significant.

Figure 18 is a schematic drawn with *lead* = 30° and *tilt* = 15°, where $O_{F(i+1)}'$ and $Z_{T(i+1)}'$ represent the cutter contact point and tool axis vector at time t_{i+1} without considering the tool path torsion, respectively, and the other symbols have the same meaning as in Section 2.2. It can be observed that under this cutter orientation, the tool path torsion increases the material removal.

According to Eqs. (23) and (28), $\omega_{Fx} = \tau_i$ (where $\dot{\theta}_i = 0$). Therefore, considering the tool path torsion τ_i, ω_{Fx} increases. At this time, since $\mathbf{r}_F = [0 \quad 0 \quad -3.9]$, the orthogonal position vector $\mathbf{r}_F$ is located below the tool. Hence, the increase of ω_{Fx} enhances the deflection motion of the tool towards the workpiece, and expands the CWE boundary, which leads to the increase of the material removal and the average cutting force, and changes the phase of the cutting forces.

6.3 Influence of cutter-orientation change on cutting force

In order to analyze the influence of cutter-orientation change on the cutting force, the pitch was set as $P = 0$. Figures 19 and 20 describes the influence of the lead angle change and the tilt angle change on cutting force;

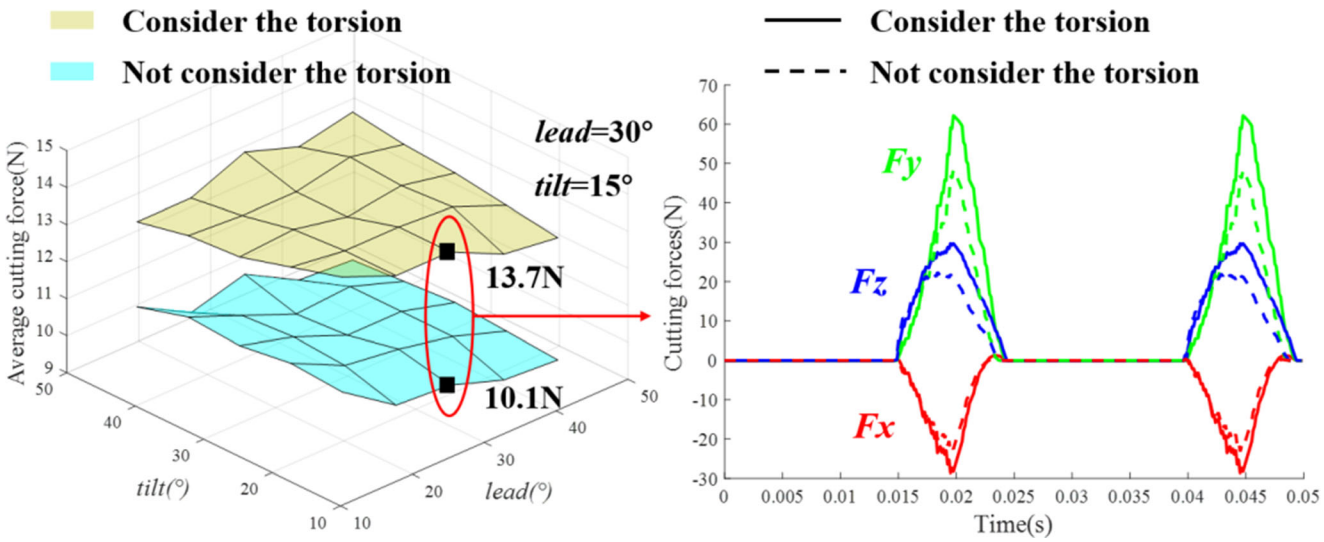

Fig. 17 Influence of the tool path torsion on cutting force

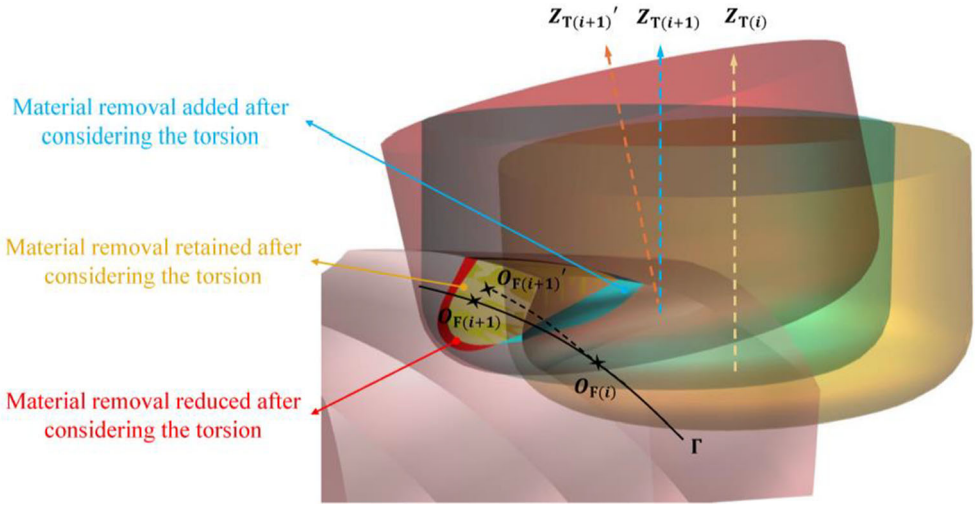

Fig. 18 Influence of the tool path torsion on cutting process

it can be seen that when the lead or tilt angle is small, the increase of inclination angle will make the decrease of the average cutting force. With the increase of cutter inclination angles, the influence of lead angle change $\dot{l}$ or tilt angle change $\dot{t}$ on average cutting force decreases rapidly.

Figure 21 is a schematic drawn with *lead* = 0°(/15°) and *tilt* = 15°(/0°), where $O_{F(i+1)}'$ and $Z_{T(i+1)}'$ represent the cutter contact point and tool axis vector at time t_{i+1} without considering the change of the lead (/tilt) angle, respectively, and the other symbols have the same meaning as in Section 2.2.

According to Eqs. (26) and (28), the lead angle change $\dot{l}$ affects ω_{Fy}, ω_{Fz}, and the speed of tool translation in all directions. It can be seen in conjunction with Fig. 21 that $\dot{l}$ greatly weakens the tool motion in the feed direction, resulting in the reduction of the material removal and IUCT, which in turn reduces the average cutting force. The influence of $\dot{l}$ on $[V_F]$ is complicated, and it is difficult to analyze its influence on the rotation or translation of the tool in a single direction.

According to Eqs. (26) and (28), the $\dot{t}$ angle change $\dot{t}$tilt increases ω_{Fx} and affects the speed of tool translation in all directions. Further calculation shows that $\mathbf{r}_F = [0 \quad 0 \quad -3.1]$, the orthogonal position vector $\mathbf{r}_F$ is located below the tool. Therefore, the increase of ω_{Fx} causes the deflection motion of the tool towards the workpiece, and meanwhile, due to $D > 0$, $\dot{t}$ enhances the tool motion in $+Y_F$-axis, that is, the lateral offset motion of the tool to the non-workpiece side. It can be seen from Fig. 22 that the lateral offset motion is stronger than the deflection motion, so the tool is still offset to the non-workpiece side on the whole. Hence, here, $\dot{t}$ narrows the CWE boundary, which leads

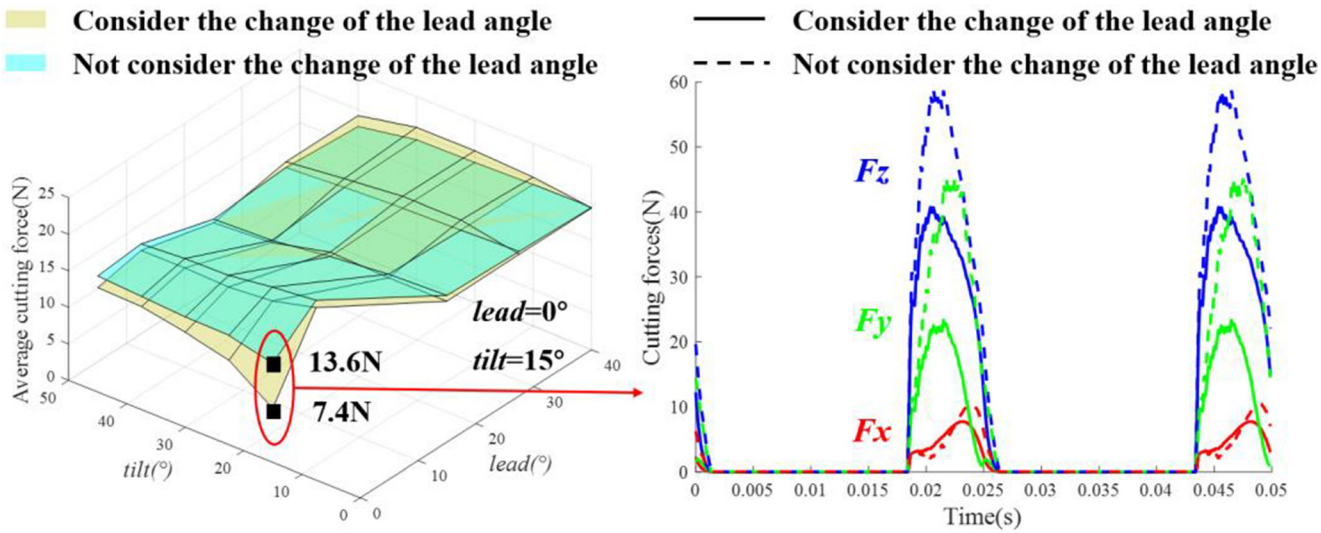

Fig. 19 Influence of the change of the lead angle on cutting force

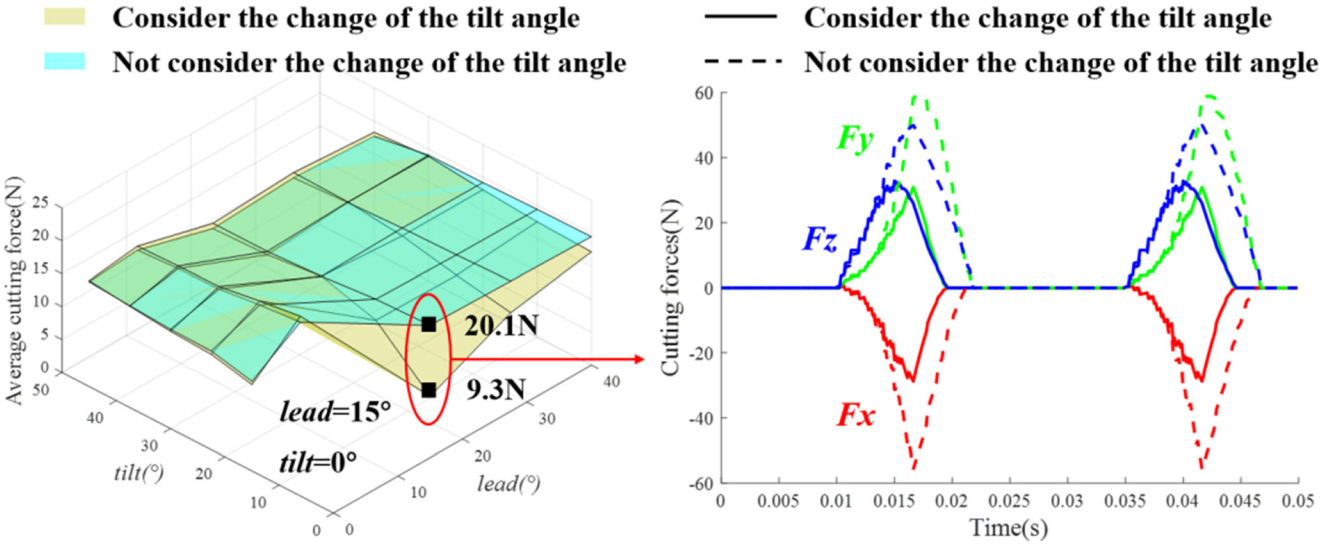

Fig. 20 Influence of the change of the tilt angle on cutting force

to the reduction of the material removal and the average cutting force and changes the phase of the cutting forces. In addition, since E in Eq. (26) is relatively large when the tool inclination is small, $\dot{t}$ weakens the average cutting force more at this time.

7 Conclusions

In this paper, a cutting force prediction method considering the tool path curvature and torsion, and cutter-orientation is proposed based on the screw theory. Firstly, the screw model is established to accurately describe the instantaneous motion of the tool considering the tool path curvature and torsion, and cutter-orientation change. The IUCT and cutter envelope surface are determined based on the screw, and then used to determine the CWE and update the workpiece surface, respectively. It should be noted that all of the above methods take into account the effects of the tool path curvature and torsion, and cutter-orientation change through the screw model.

From the simulation results, it can be seen that, under the designed conditions, the tool path curvature and lead angle change mainly affect the IUCT by affecting the tool motion in the feed direction, while the tool path torsion and tilt angle change mainly affect the CWE by affecting the lateral offest motion of the tool. Therefore, the tool path curvature and torsion, and cutter-orientation change can affect the cutting force by affecting the tool motion, which can be observed through the screw model.

The five-axis cutting force prediction model in this paper is very suitable for tool trajectory planning of sculptured surface parts, or any other situation involving

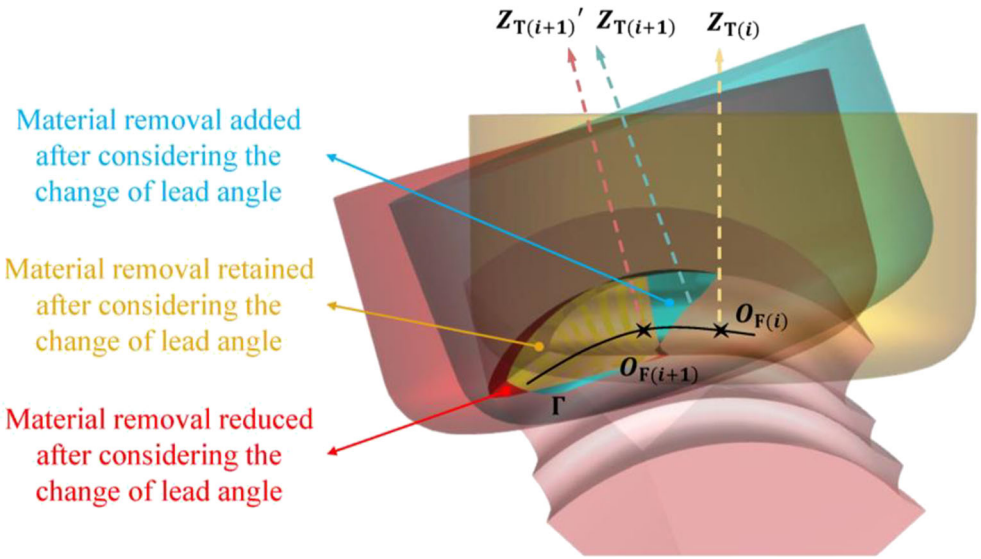

Fig. 21 Influence of the change of the lead angle on cutting process

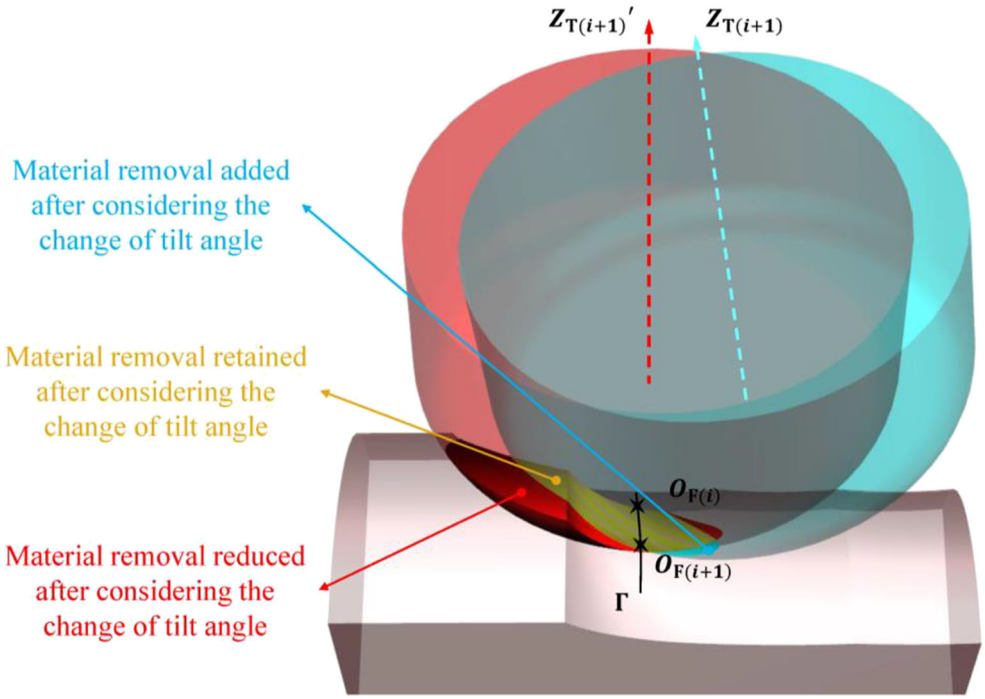

Fig. 22 Influence of the change of the tilt angle on cutting process

a great degree of the tool path curvature and torsion, and cutter-orientation change and requiring high-precision of cutting force prediction. However, this study does not consider cutter runout, cutter vibration, etc.; how to take advantage of the screw theory to analyze these factors and further apply it to process parameter optimization are still problems to be solved.

Authors' contributions Zerun Zhu proposed the article's innovative thinking, derived the core formula of the article, and provided the experimental design. Jiawei Wu perfected the formula derivation and wrote the code, and completed model validation and the writing of the article. Fangyu Peng and Rong Yan putted forward many constructive suggestions for the writing of the whole article, while Xiaowei Tang putted forward some constructive suggestions for the experimental part.

Funding This work was supported by the National Natural Science Foundation of China under Grant No. 51775213, National Natural Science Foundation of China under Grant No. 91860206, and National Science Fund for Distinguished Young Scholars under Grant No. 51625502.

Data availability Milling force raw data for force coefficients calibration and model verification used during the study are available from the corresponding author by request, and other related materials can also be obtained from the corresponding author.

Compliance with ethical standards

Ethical approval Not applicable.

Consent to participate All authors and facilitators have certified their participation in this work.

Consent to publish All authors certify that they consent to publish the article. The article is the author's original work and has not been published in advance or considered for publication elsewhere.

Conflict of interest The authors have no relevant financial or non-financial interests to disclose.

The authors have no conflicts of interest to declare that are relevant to the content of this article.

All authors certify that they have no affiliations with or involvement in any organization or entity with any financial interest or non-financial interest in the subject matter or materials discussed in this manuscript.

Code availability The code for milling force coefficients calibration and model verification during the study is available from the corresponding author by request.

References

1. Ning J, Zhu L (2019) Parametric design and surface topography analysis of turbine blade processing by turn-milling based on CAM. Int J Adv Manuf Technol 104(9-12):3977–3990
2. Luo M, Hah C, Hafeez HM (2019) Four-axis trochoidal toolpath planning for rough milling of aero-engine blisks. Chin J Aeronaut 32(8):2009–2016
3. Dongming G, Fei R, Yuwen S (2010) An approach to modeling cutting forces in five-axis ball-end milling of curved geometries based on tool motion analysis. J Manuf Sci Eng-Trans ASME 132(4)
4. Ozturk E, Tunc LT, Budak E (2009) Investigation of lead and tilt angle effects in 5-axis ball-end milling processes. Int J Mach Tools Manuf 49(14):1053–1062
5. Duan X, Peng F, Zhu K, Jiang G (2019) Tool orientation optimization considering cutter deflection error caused by cutting force for

multi-axis sculptured surface milling. Int J Adv Manuf Technol 103(5-8):1925–1934
6. Zhu Z, Peng F, Yan R, Li Z, Wu J, Tang X, Chen C (2020) Influence mechanism of machining angles on force induced error and their selection in five axis bullnose end milling. Chin J Aeronaut. https://doi.org/10.1016/j.cja.2019.12.019
7. Zhu Z, Yan R, Peng F, Duan X, Zhou L, Song K, Guo C (2016) Parametric chip thickness model based cutting forces estimation considering cutter runout of five-axis general end milling. Int J Mach Tools Manuf 101:35–51
8. Fussell BK, Jerard RB, Hemmett JG (2003) Modeling of cutting geometry and forces for 5-axis sculptured surface machining. Comput Aided Des 35(4):333–346
9. Wang L, Si H, Gu L (2019) Prediction of cutting forces in flank milling of parts with non-developable ruled surfaces. Chin J Aeronaut 32(7):1788–1796
10. Duan X, Peng F, Zhu Z, Jiang G (2019) Cutting edge element modeling-based cutter-workpiece engagement determination and cutting force prediction in five-axis milling. Int J Adv Manuf Technol 102(1-4):421–430
11. Wu B, Yan X, Luo M, Gao G (2013) Cutting force prediction for circular end milling process. Chin J Aeronaut 26(4):1057–1063
12. Zhu RX, Kapoor SG, DeVor RE (2001) Mechanistic modeling of the ball end milling process for multi-axis machining of free-form surfaces. J Manuf Sci Eng-Trans ASME 123(3):369–379
13. Sun Y, Ren F, Guo D, Jia Z (2009) Estimation and experimental validation of cutting forces in ball-end milling of sculptured surfaces. Int J Mach Tools Manuf 49(15):1238–1244
14. Li Z-L, Niu J-B, Wang X-Z, Zhu L-M (2015) Mechanistic modeling of five-axis machining with a general end mill considering cutter runout. Int J Mach Tools Manuf 96:67–79
15. Wojciechowski S, Mrozek K (2017) Mechanical and technological aspects of micro ball end milling with various tool inclinations. Int J Mech Sci 134:424–435
16. Wojciechowski S, Matuszak M, Powałka B, Madajewski M, Maruda RW, Królczyk GM (2019) Prediction of cutting forces during micro end milling considering chip thickness accumulation. Int J Mach Tools Manuf 147:103466
17. Zhu Z, Peng F, Yan R, Song K, Li Z, Duan X (2017) High efficiency simulation of five-axis cutting force based on the symbolically solvable cutting contact boundary model. Int J Adv Manuf Technol 94(5-8):2435–2455
18. Larue A, Altintas Y (2005) Simulation of flank milling processes. Int J Mach Tools Manuf 45(4-5):549–559
19. Lazoglu I, Boz Y, Erdim H (2011) Five-axis milling mechanics for complex free form surfaces. CIRP Ann 60(1):117–120
20. Erdim H, Sullivan A (2013) Cutter workpiece engagement calculations for five-axis milling using composite adaptively sampled distance fields. Procedia CIRP 8:438–443
21. Altintas Y, Kersting P, Biermann D, Budak E, Denkena B, Lazoglu I (2014) Virtual process systems for part machining operations. CIRP Ann 63(2):585–605
22. Kiswanto G, Hendriko H, Duc E (2014) An analytical method for obtaining cutter workpiece engagement during a semi-finish in five-axis milling. Comput Aided Des 55:81–93
23. Kim Y-H, Ko S-L (2005) Improvement of cutting simulation using the octree method. Int J Adv Manuf Technol 28(11-12):1152–1160
24. Zhang L (2011) Process modeling and toolpath optimization for five-axis ball-end milling based on tool motion analysis. Int J Adv Manuf Technol 57(9-12):905–916
25. Wei ZC, Wang MJ, Zhu JN, Gu LY (2011) Cutting force prediction in ball end milling of sculptured surface with Z-level contouring tool path. Int J Mach Tools Manuf 51(5):428–432
26. Cao Q, Xue D, Zhao J, Li Y (2010) A cutting force model considering influence of radius of curvature for sculptured surface machining. Int J Adv Manuf Technol 54(5-8):821–835
27. Yuan M, Wang X, Jiao L, Yi J, Liu S (2017) Prediction of dimension error based on the deflection of cutting tool in micro ball-end milling. Int J Adv Manuf Technol 93(1-4):825–837
28. Ruibo H, Yingjun Z, Shunian Y, Shuzi Y (2010) Kinematic-Parameter Identification for Serial-Robot Calibration Based on POE Formula. IEEE Trans Robot 26(3):411–423
29. Yang X, Wu L, Li J, Chen K (2014) A minimal kinematic model for serial robot calibration using POE formula. Robot Comput Integr Manuf 30(3):326–334
30. Yang J, Mayer JRR, Altintas Y (2015) A position independent geometric errors identification and correction method for five-axis serial machines based on screw theory. Int J Mach Tools Manuf 95: 52–66
31. Yang J, Huang T, Yang M, Ding H, Zhang H-T (2016) Generalized cutting loads decomposition model of five-axis serial machine tools based on the screw theory. Int J Adv Manuf Technol 91(1-4):399–410
32. Gong H, Wang N (2009) Analytical calculation of the envelope surface for generic milling tools directly from CL-data based on the moving frame method. Comput Aided Des 41(11):848–855
33. Zhebo Z (2014) Engineering Differential Geometry. Peking University Press, Beijing
34. Wan M, Zhang WH, Qin GH, Tan G (2007) Efficient calibration of instantaneous cutting force coefficients and runout parameters for general end mills. Int J Mach Tools Manuf 47(11):1767–1776
35. Wojciechowski S (2015) The estimation of cutting forces and specific force coefficients during finishing ball end milling of inclined surfaces. Int J Mach Tools Manuf 89:110–123